Networks and Heterogeneous Media

https://www.aimspress.com/journal/nhm

NHM, 20(4): 1292–1332.
DOI: 10.3934/nhm.2025056
Received: 28 March 2025
Revised: 07 November 2025
Accepted: 21 November 2025
Published: 05 December 2025

Research article

Kinetic modeling approach for a heterogeneous neuronal network activity using adjacency matrices

M. Menale[1,*], C. Tribuzi[2], R. Shah[1], C. A. Lupascu[3] and A. Marasco[1,3]

[1] Department of Mathematics and Applications, University of Naples Federico II, Naples, Italy

[2] Nova Analysis, Brescia, Italy

[3] Institute of Biophysics, National Research Council, Palermo, Italy

* **Correspondence:** Email: marco.menale@unina.it.

Abstract: The heterogeneity of neuronal networks plays a crucial role in shaping emergent dynamics. In this work, we introduced a kinetic modeling approach to describe the activity of heterogeneous neuronal networks through transition probabilities and adjacency matrices. The model explicitly accounts for both structural and functional heterogeneity by considering two interacting neuronal populations—excitatory pyramidal neurons and inhibitory interneurons—distributed across network slices. The transition probabilities encode the binary stochastic interactions between neurons, capturing both the neuronal types involved (excitatory or inhibitory) and the connectivity structure within and between slices. Complementarily, adjacency matrices define the weighted connections among neurons, specifying the structural organization of each slice and the interactions across slices. Together, these two components characterize the functional and the structural heterogeneity of the system. From this framework, we derived a system of nonlinear ordinary differential equations describing the mesoscopic dynamics of the network. First, for the one-slice model, we provided analytical results on the existence and stability of equilibrium states. Then, we presented numerical simulations for two- and four-slice networks to investigate the role of functional and structural heterogeneity. In particular, after defining the excitatory-, inhibitory-, and balanced count regimes and introducing an a priori criterion for their identification, we demonstrated how heterogeneity influences both the short- and long-term dynamics of the network. Our findings revealed that increasing heterogeneity not only alters the proportion of active neurons but also induces more complex dynamical behaviors, potentially driving shifts between excitatory-count- and inhibitory-count-dominated regimes.

Keywords: mathematical modeling; stochastic interactions; network connectivity; inhibitory- and excitatory-count-dominated network regimes; external inputs

1. Introduction

The brain can be modeled as a complex network composed of billions of interacting neurons. The result of such non-linear interactions is the emergence of intricate spatio-temporal patterns of neuronal activity, which underlie fundamental processes such as cognition, perception, action, and behavior (see [1] and the references therein). Furthermore, these networks exhibit significant neuron-to-neuron heterogeneity in their physiological properties, firing dynamics, and connectivity structure, contributing to the diversity and adaptability of brain function.

Over the past decades, mathematical modeling has become an essential tool for investigating large-scale brain dynamics and uncovering potential critical phenomena underlying brain activity [1]. The main sources of variability among these models emerge at the microscopic level, reflecting differences both in the biophysical description of single-neuron dynamics and in the structural organization of neuronal connectivity. In the brain, neurons exhibit complex and highly variable firing patterns that critically shape network dynamics. Morphologically and biophysically detailed Hodgkin-Huxley-type models can accurately reproduce these patterns [2–4], but they incur substantial computational costs, making them impractical for large-scale network implementations. Therefore, simplified neuron models, such as integrate-and-fire [5–9] or Izhikevich neurons [10, 11], are widely adopted to simulate extended networks across multiple brain regions. A relevant question concerns how these simplified models can capture neuron-to-neuron heterogeneity and still generate biologically realistic dynamics, especially since most of them are not constrained by experimental data. In this context, a notable approach is provided by adaptive generalized leaky integrate-and-fire (A-GLIF) models, which overcome these limitations by accurately reproducing experimental spike timing under both constant and variable current inputs, while enabling the generation of large populations of CA1 pyramidal neurons and interneurons that capture the full range of observed firing dynamics for large-scale network simulations [12–14]. Overall, the literature often reproduces only a limited neuron-to-neuron heterogeneity; for instance, in [11] a network of 90,000 neurons is modeled using only eight distinct Izhikevich neuron models. Nevertheless, this level of simplification is often sufficient to capture relevant macroscopic network dynamics.

Another relevant line of research focuses on spiking-network models based on kinetic and mean-field approaches [7, 8, 15–19]. In these models, neuron-to-neuron heterogeneity is generally introduced through variability in spike thresholds [20], synaptic conductances [5, 6], or adaptation and excitability parameters [7, 21–23], among others. When the focus is on *collective network dynamics*, it is therefore reasonable to adopt minimal models with simplified forms of population heterogeneity which, despite lacking detailed microscopic realism, are still able to capture the essential macroscopic behaviors.

In this work, we adopt this perspective and investigate the *collective neuronal dynamics* emerging from the intrinsic properties of the network. In particular, rather than employing biophysically detailed neuron models, we use a (simplified) kinetic framework that reproduces macroscopic behavior driven solely by intrinsic network properties, such as the topology of the connectivity structure and microscopic interactions governed within a probabilistic framework. This modeling strategy is well-established in the literature, as models incorporating basic properties of biological neuronal networks have been employed to investigate collective oscillations [24], metastability [25], multistability [20], asynchronous states and Griffiths phases [26, 27], and other related phenomena. For instance, in [24], a network consisting of both excitatory and inhibitory neurons was considered, with the *adjacency matrix* employed to define

the connectivity of the network. Furthermore, the oscillatory collective dynamics were analyzed in the presence of an external stimulus train, representing inputs from either other regions of the nervous system or external sources. Specifically, at each time step, a fraction of neurons fires randomly and the study explored the temporal evolution of active neuron density and the emergence of network oscillations, also accounting for structural variations. However, the brain is spontaneously active even in the absence of external inputs (see [28], and the references therein), whereas, this model is unable to capture the spontaneous network activity that reflects intrinsic properties, such as local connectivity and the individual characteristics of neurons. Other models, ranging from simple rate-based models of binary neurons, where activation is probabilistically determined by a transfer function dependent on weighted inputs [26, 29], to mean-field models [20, 30], investigate the collective dynamics of neuronal heterogeneous networks.

As previously discussed, network heterogeneity encompasses both neuronal populations (primarily excitatory and inhibitory neurons) and the connectivity structure. In neuronal populations, heterogeneity can arise from differences in electrophysiological properties among neurons of the same type, as well as from variations in the relative proportions of excitatory and inhibitory neurons [11], both of which affect the overall excitation-inhibition balance. To explore the effects of within-type heterogeneity on network dynamics, it is common to assume all-to-all connectivity [20]. However, the connectivity architecture of a heterogeneous network is at least as important as the heterogeneity within and between neuronal populations in shaping network dynamics [16, 17]. Nevertheless, the cumulative effects of these heterogeneous characteristics influence macroscopic network dynamics in an unpredictable manner. For these reasons, the structure of network connectivity has been extensively studied and developed for several aims. For instance, in the context of neuronal synchronization, as explored in [31], connectivity patterns have been designed based on the well-known Watts-Strogatz small-world network model [32], which interpolates between nearest-neighbor and random connectivity. Network heterogeneity is also manifested through varying densities of excitatory and inhibitory neurons, which leads to the emergence of a spatial architecture where certain regions become more or less prone to generating firing activity due to a locally increased or decreased excitatory/inhibitory ratio [26]. Other influential approaches include models based on *graph theory* (see [33–35], and the references therein) and scale-free networks characterized by highly connected hub cells [36]. Over the years, these studies have underscored the significant impact of connectivity structure on the complex dynamics of the brain (see [31, 33], and the references therein). To provide a comprehensive mathematical description of connectivity, adjacency matrices are commonly used [24, 37]. These matrices offer a compact and structured representation of node connections [38, 39], and allow the use of linear algebra and spectral methods to extract key network features such as connectivity, centrality, and community structure [40].

The kinetic theory approach employed in this work to model the evolution of a neuronal network has gained considerable attention in recent years, due to its versatility in providing a multiscale description of the phenomenon under investigation, encompassing the microscale, mesoscale, and macroscale, see, e.g., [41, pp. 3–9] and the references therein. In particular, we refer to the active particles method [42], following its established applications in biological contexts [43, 44], and we focus here on binary interactions rather than multiple ones. This choice is further supported by recent advances in neuroscience modeling based on kinetic theory [5, 6, 9, 45, 46] and the mean-field approach [7, 8, 15–19].

First, the overall system is divided into *functional subsystems*, which implicitly describe both the spatial structure of the network and its functional specialization. In particular, we consider a layered

organization, where each functional subsystem—referred to as a *slice*—includes both inhibitory and excitatory neuron populations, each characterized by similar electrophysiological properties [47–51], while also implicitly defining the spatial extent of the network. This organization can reflect specific anatomical or functional structures, such as longitudinal or transverse slices of variable thickness supporting signal propagation along preferential pathways [14], or the grouping of homogeneous neuronal subtypes—e.g., interneuron classes (AA, BP, BS, CCKBC, IVY, NGF, etc.) [52] and pyramidal neurons with similar firing characteristics. At the microscopic level, each unit is modeled as an active particle [42], where the activity is assumed to be discrete [53], representing either firing or silent neurons within the inhibitory and excitatory populations. The evolution of the system is then governed by stochastic binary interactions, consisting of four types of asymmetrical interactions: pyramidal-to-pyramidal, pyramidal-to-interneuron, interneuron-to-interneuron, and interneuron-to-pyramidal. To provide a more realistic description of the phenomenon, specific *weights* are introduced, as the activity of the neurons and the evolution of the whole network depend on the connections of each neuron. These weights mimic the role of adjacency matrices, which are commonly employed in more general kinetic frameworks. At the mesoscopic scale, we then describe the evolution of the discrete distribution functions associated with the functional subsystems. Since the microscopic state variable is discrete in each functional subsystem, the kinetic formulation naturally leads to a finite system of nonlinear ordinary differential equations, each governing the time evolution of the corresponding discrete distribution function, as first shown in [53], and later applied to real-world cases, e.g., [54]. This constitutes the kinetic level of the description. At the macroscopic level, the system is considered in its entirety, focusing on the moments of the distributions. The derivation of macroscopic models directly from the underlying kinetic description represents a significant and challenging problem (see [55, 56], and the references therein). Therefore, a kinetic modeling framework is adopted to describe a network composed of interneurons and pyramidal neurons, where adjacency matrices are used to model the weights between pairs of connections. As in [26, 30, 37], we analyze how homogeneous and heterogeneous connectivity structures, along with the heterogeneity of inhibitory and excitatory neuron populations, affect network dynamics in terms of the number of active interneurons and pyramidal neurons over time, both globally and within each slice.

Despite the general description of network activity provided by this kinetic framework, a mathematical analysis of the model can only be performed when the activity of the entire network is considered. Furthermore, designing, simulating, and analyzing large heterogeneous networks with a focus on architectural complexity is not straightforward, even in a numerical simulation environment. Then, in this paper, we restrict our numerical investigations to models composed of one, two, and four slices, defining interactions between neurons either within the same slice (within-type) or across different slices (between-type) using simplified adjacency matrices, which provide a concise representation of the network connectivity. Specifically, these matrices do not explicitly determine each individual connection but instead offer a statistical description of the connectivity in terms of percentages. Nevertheless, even within this simplified version of the kinetic model, we are able to highlight the role of connectivity structure and neuronal population heterogeneity in shaping network dynamics, both at a global scale and within individual slices. In this context, we introduce the concepts of *inhibitory-count-dominated* and *excitatory-count-dominated* regimes, referring to network states in which inhibitory (interneurons) or excitatory (pyramidal) neurons, respectively, constitute the predominant fraction of active neurons over a given time interval. We further introduce the

inhibition-count and excitation-count rates and propose a method to determine a priori whether the network operates in an inhibitory- or excitatory-count-dominated regime, based on the relative magnitudes of these rates. Although this result is analytically proven only for the one-slice model, it is fully supported by all numerical simulations presented in this work. Notably, both the inhibition- and excitation-count rates are intrinsic network properties of the network, i.e., they are independent of external inputs and depend solely on the connectivity structure and the functional properties of the neuronal populations. A related notion is proposed in [57], where a network of excitatory and inhibitory neurons—each in either an active or inactive state—is considered, and activation and deactivation rates are defined as functions of the surrounding neighborhood.

Overall, introducing heterogeneity into the connectivity structure leads to more intricate dynamical behavior and enhances the phenomenological richness of the system, compared to homogeneous or fully connected (all-to-all) network configurations. Moreover, as connectivity heterogeneity increases, the network activity involves a smaller number of active neurons and may potentially drive a transition from an excitatory-count-dominated to an inhibitory-count-dominated regime, and vice versa. Although the present study focuses on the intrinsic dynamics of the network, we also perform numerical simulations in which a fraction of neurons—either across the whole network or confined to a single slice—is activated by external inputs representing signals from other brain regions. Under this condition, the network dynamics exhibit oscillatory patterns driven by the frequencies and strength of the external inputs.

The number (or fraction) of active neurons analyzed in this work is a widely used metric for characterizing global network activity and emergent collective phenomena [24, 58–66]. This measure has been employed to quantify avalanche sizes during pattern recognition [58], assess inhibitory effects on network dynamics [59], and describe steady states, oscillations, and avalanches in stochastic models of active and inactive neuron populations [60], including formulations based on Langevin-type Wilson–Cowan equations [61]. Such a coarse-grained representation enables scalable analyses of large neuronal populations, facilitating the analysis of network stability [62], oscillatory regimes [63], and pathological conditions such as seizures [64] and Huntington's disease [65]. It also allows quantifying the storage capacity of neural networks [66], where neurons are either active or inactive and memory performance depends on the number of active units. Furthermore, the number of active neurons can be directly inferred from experimental recordings using techniques such as calcium imaging, electroencephalogram (EEG), or functional magnetic resonance imaging (fMRI), which capture population-level activity rather than single-neuron dynamics. For instance, calcium imaging detects neuronal activation by monitoring fluorescent signals associated with transient increases in intracellular calcium [67], while EEG and fMRI measure aggregate activity over large populations and extended time windows, reflecting global network states rather than individual spikes [68]. Consequently, quantifying the number or fraction of active neurons improves correspondence with experimental data, enabling robust model–data integration.

The paper is structured as follows. After the introduction, Section 2 discusses the kinetic approach for modeling heterogeneous neuronal networks, composed of S slices containing both interneurons and pyramidal neurons. Section 3 examines a simplified version of the model, where connections within and between slices are described in percentage terms. Specifically, the first subsection analyzes the one-slice model and provides a stability analysis of the equilibria. The two subsequent subsections address the two-slice and four-slice models, respectively, where network properties are investigated through numerical simulations. The final subsection of Section 3 addresses the case of external input.

We conclude with some remarks and perspectives for future research.

2. A kinetic approach for a heterogeneous neuronal network

This section is devoted to the derivation of the kinetic model for a heterogeneous neuronal network. We adopt the discrete kinetic approach of [53, 69], introducing some novel extensions tailored to the present modeling framework. In particular, we address network heterogeneity in terms of both neuron populations, which refers to the functionality, and of connectivity structure. First, we assume two populations of interacting cells: *interneurons*, which have an inhibitory effect, and *pyramidal neurons*, which have an excitatory effect. From a kinetic modeling perspective, these two populations constitute the fundamental units of every functional subsystem. For the purposes of this paper, the total number of neurons (interneurons and pyramidal neurons) N is assumed to remain constant over time, as nonconservative events do not occur.

The overall network is divided into S *slices*, $S \in \mathbb{N}$. The introduction of slices serves a dual purpose introducing heterogeneity into the network. On one hand, slices can group neuron populations by *cell types* [47–51] or by similar firing dynamics, such as adapting, non-adapting, and bursting neurons [70]. On the other hand, slices can represent the spatial extension of the network, at least in a discrete formulation, where each slice acts as a small specialized region within a neuronal area.

Therefore, each neuron belongs to a specific slice, and each slice may contain both interneurons and pyramidal neurons. For each slice $h \in \{1, 2, \dots, S\}$, there is a certain number of neurons, denoted as n_h. Moreover, the neurons from 1 to $\hat{h}$ are interneurons, whereas neurons from $\hat{h}+1$ to n_h are pyramidal neurons. If $n_{h,\text{int}}$ and $n_{h,\text{pyr}}$ represent the number of interneurons and pyramidal neurons, respectively, in slice h, then

$$n_{h,\text{int}} = \hat{h}, \quad n_{h,\text{pyr}} = n_h - \hat{h}.$$

Bearing all the above in mind, for each slice h, with $h \in \{1, 2, \dots, S\}$, each neuron can be characterized by the integer r, where $r \in \{1, 2, \dots, \hat{h}-1, \hat{h}, \hat{h}+1, \dots, n_h\}$, which refers to both the position within the slice and the functional subsystem. Specifically, if the neuron is an interneuron, $1 \le r \le \hat{h}$, and if it is a pyramidal neuron, $\hat{h}+1 \le r \le n_h$. Hereafter, we will refer to r as the *label* of the neuron for each slice. Thus, the pair (h, r) provides a preliminary spatial-functional characterization of each neuron in the network specifying its slice, position, and functional class (either interneuron or pyramidal neuron). It is worth noting that the label (h, r) does not change during the evolution of the network since the overall structure is conservative, i.e., proliferative or destructive events do not occur.

Neuronal subtypes and their positions within the slices provide an initial description of the network at the microscopic level. Now, we introduce the activity variable for this model, represented by neuronal subtypes and the *somatic membrane potential* v of each neuron. In general, this latter quantity may take values in a continuous subset of $\mathbb{R}$. A neuron fires an action potential, i.e., a spike event occurs, when the membrane potential v reaches a threshold value v_{th}. For the purposes of this paper, we are only interested in whether the membrane potential exceeds this threshold or not. Therefore, we assume that v can only take two possible values, i.e.,

$$v \in \{v_0, v_1\} = \{0, 1\}.$$

Specifically, if $v = v_0 = 0$, the membrane potential of the neuron is below the threshold and no spike event occurs; in this case, we say that the neuron is *inactive*. Conversely, if $v = v_1 = 1$, the membrane

potential exceeds the threshold, triggering a spike event; in this case, we say that the neuron is *active*. Although the binary state $\{0, 1\}$ might suggest that this assumption applies only to neuronal populations exhibiting bistable membrane potentials, such as striatal projection neurons, it is employed here instead as a general coarse-grained representation of neuronal activity, distinguishing neurons that are active (i.e., have emitted at least one spike within the considered time window) from those that are inactive (i.e., whose membrane potential remains below a threshold). This modeling choice is well-established and has been widely adopted in the literature on stochastic network models [59–61, 66, 71].

Finally, bearing all the above in mind, at the microscopic scale, a neuron is characterized by the discrete triplet $(h,\ r,\ v_l)$. It is worth pointing out that the potential v_l is the only quantity that can change during the evolution of the system, as position and functionality cannot. Then, we assume that the microscopic dynamics follow a kinetic binary scheme. A neuron in the microscopic state (h, r, v_n) (where $h \in \{1, 2, \dots, S\}$ is the slice, $r \in \{1,\ 2, \dots, \hat{h} - 1,\ \hat{h},\ \hat{h} + 1, \dots, n_h\}$ is the label, and $v_n \in \{0, 1\}$ is the potential) passes into the state (h, r, v_l) after interacting with a neuron in the microscopic state (k, s, v_m). Due to these interactions, a neuron can only change the value of its potential. To model the microscopic dynamics, we introduce the *transition probability* $C^{rs}_{hk}(v_l, v_n, v_m)$, where $h, k \in \{1, 2, \dots, S\}$, $r \in \{1,\ 2, \dots, \hat{h} - 1,\ \hat{h},\ \hat{h} + 1, \dots, n_h\}$, $s \in \{1,\ 2, \dots,\ \hat{k} - 1,\ \hat{k},\ \hat{k} + 1, \dots, n_k\}$, and $l, n, m \in \{0,\ 1\}$. In particular, $C^{rs}_{hk}(v_l, v_n, v_m)$ provides the probability that a neuron in the microscopic state (h, r, v_n) passes into the state (h, r, v_l) after interacting with a neuron in the microscopic state (k, s, v_m), as depicted in Figure 1. Hereafter, we refer to the neuron in the microscopic state (h, r, v_n) as the *first neuron*, and to the neuron in the microscopic state (k, s, v_m) as the *second neuron*. The second neuron acts on the first neuron according to its functionality.

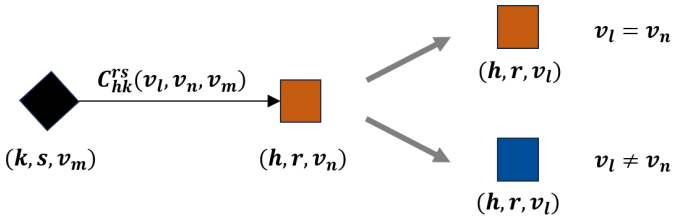

Figure 1. Binary microscopic interaction. A neuron in the microscopic state (h, r, v_n) undergoes a transition to the state (h, r, v_l) after interacting with a neuron in the microscopic state (k, s, v_m), with a transition probability $C^{rs}_{hk}(v_l, v_n, v_m)$.

Since a probability structure is assumed, the following assumption holds true:

H1. For all $h, k \in \{1, 2, \dots, S\}$, $r \in \{1,\ 2, \dots, \hat{h}-1,\ \hat{h},\ \hat{h}+1, \dots, n_h\}$, $s \in \{1,\ 2, \dots,\ \hat{k}-1,\ \hat{k},\ \hat{k}+1, \dots, n_k\}$, and $n, m, l \in \{0, 1\}$,

$$\sum_{l=0}^{1} C^{rs}_{hk}(v_l, v_n, v_m) = C^{rs}_{hk}(0, v_n, v_m) + C^{rs}_{hk}(1, v_n, v_m) = 1. \tag{2.1}$$

Furthermore, the transition probability $C^{rs}_{hk}(v_l, v_n, v_m)$ can be further specified as follows:

H2. Let $(v_n, v_m) = (0,\ 0)$, i.e., the two interacting neurons are both inactive. Then, for all $h, k \in \{1, 2, \dots, S\}$, $r \in \{1,\ 2, \dots, \hat{h} - 1,\ \hat{h},\ \hat{h} + 1, \dots, n_h\}$, and $s \in \{1,\ 2, \dots,\ \hat{k} - 1,\ \hat{k},\ \hat{k} + 1, \dots, n_k\}$, such

that $(h, r) \neq (k, s)$, we have

$$C_{hk}^{rs}(v_l, 0, 0) = \begin{cases} 1 & v_l = 0, \\ 0 & v_l = 1. \end{cases} \tag{2.2}$$

H3. Let $(v_n, v_m) = (1, 0)$, i.e., the second neuron (which could either inhibit or excite the first neuron) is inactive. In this case, no change occurs, and the first neuron remains active. Then, for all $h, k \in \{1, 2, \ldots, S\}$, $r \in \{1, 2, \ldots, \hat{h}-1, \hat{h}, \hat{h}+1, \ldots, n_h\}$, and $s \in \{1, 2, \ldots, \hat{k}-1, \hat{k}, \hat{k}+1, \ldots, n_k\}$, such that $(h, r) \neq (k, s)$, we obtain

$$C_{hk}^{rs}(v_l, 1, 0) = \begin{cases} 0 & v_l = 0, \\ 1 & v_l = 1. \end{cases} \tag{2.3}$$

H4. Let $(v_n, v_m) = (0, 1)$. In this case, the first neuron, which can change its potential state due to the binary interaction, is inactive, while the second neuron is active. In general, the transition probability follows this scheme, for all $h, k \in \{1, 2, \ldots, S\}$, $r \in \{1, 2, \ldots, \hat{h}-1, \hat{h}, \hat{h}+1, \ldots, n_h\}$, and $s \in \{1, 2, \ldots, \hat{k}-1, \hat{k}, \hat{k}+1, \ldots, n_k\}$, such that $(h, r) \neq (k, s)$:

$$C_{hk}^{rs}(v_l, 0, 1) = \begin{cases} 1 - p_{hk}^{rs} & v_l = 0, \\ p_{hk}^{rs} & v_l = 1, \end{cases} \tag{2.4}$$

where $p_{hk}^{rs} \in [0, 1]$.

The general scheme in Eq (2.4) can be further refined (see Figure 2) by considering functionalities of the involved neurons. In what follows, we simplify the notation by using x-to-y to highlight the directional interaction from neuron x to neuron y. Specifically, we have:

int-to-int In this case, the first neuron remains inactive since interneurons, being inhibitory, do not directly excite one another. Then, for $r \in \{1, 2, \ldots, \hat{h}\}$ and $s \in \{1, 2, \ldots, \hat{k}\}$:

$$C_{hk}^{rs}(v_l, 0, 1) = \begin{cases} 1 & v_l = 0, \\ 0 & v_l = 1. \end{cases} \tag{2.5}$$

pyr-to-int An active pyramidal neuron can excite an inactive interneuron. Then, for $r \in \{1, 2, \ldots, \hat{h}\}$ and $s \in \{\hat{k}+1, \hat{k}+2, \ldots, n_k\}$:

$$C_{hk}^{rs}(v_l, 0, 1) = \begin{cases} 1 - p_{1,hk}^{rs} & v_l = 0, \\ p_{1,hk}^{rs} & v_l = 1. \end{cases} \tag{2.6}$$

int-to-pyr An active interneuron cannot excite an inactive pyramidal neuron, as interneurons primarily have an inhibitory role. Then, for $r \in \{\hat{h}+1, \hat{h}+2, \ldots, n_h\}$ and $s \in \{1, 2, \ldots, \hat{k}\}$:

$$C_{hk}^{rs}(v_l, 0, 1) = \begin{cases} 1 & v_l = 0, \\ 0 & v_l = 1. \end{cases} \tag{2.7}$$

pyr-to-pyr: An active pyramidal neuron can depolarize another pyramidal neuron and trigger its activation. Then, for $r \in \{\hat{h}+1,\ \hat{h}+2, \ldots, n_h\}$ and $s \in \{\hat{k}+1,\ \hat{k}+2, \ldots, n_k\}$:

$$C^{rs}_{hk}(v_l, 0, 1) = \begin{cases} 1 - p^{rs}_{2,hk} & v_l = 0, \\ p^{rs}_{2,hk} & v_l = 1. \end{cases} \tag{2.8}$$

H5. Let $(v_n, v_m) = (1,\ 1)$, such that $(h, r) \neq (k, s)$, i.e., the two interacting neurons are both active (see Figure 2). By using the same approach of the assumption **H3**, we distinguish the following cases:

int-to-int Two active interneurons can influence each other; if inhibition is strong enough, the first neuron can turn off ($v_l = 0$); otherwise, it remains active. Then, for $r \in \{1, 2, \ldots, \hat{h}\}$ and $s \in \{1, 2, \ldots, \hat{k}\}$:

$$C^{rs}_{hk}(v_l, 1, 1) = \begin{cases} q^{rs}_{1,hk} & v_l = 0, \\ 1 - q^{rs}_{1,hk} & v_l = 1. \end{cases} \tag{2.9}$$

pyr-to-int A pyramidal neuron cannot deactivate an active interneuron; this reflects the fact that pyramidal neurons release excitatory neurotransmitters, which do not have a direct inhibitory effect on interneurons. Then, for $r \in \{1, 2, \ldots, \hat{h}\}$ and $s \in \{\hat{k}+1,\ \hat{k}+2, \ldots, n_k\}$:

$$C^{rs}_{hk}(v_l, 1, 1) = \begin{cases} 0 & v_l = 0 \\ 1 & v_l = 1. \end{cases} \tag{2.10}$$

int-to-pyr An active interneuron can deactivate a pyramidal neuron. This can represent a feedback inhibition mechanism, where an active interneuron inhibits a pyramidal neuron, reducing the overall excitatory activity in the network. Then, for $r \in \{\hat{h}+1,\ \hat{h}+2, \ldots, n_h\}$ and $s \in \{1, 2, \ldots, \hat{k}\}$:

$$C^{rs}_{hk}(v_l, 1, 1) = \begin{cases} q^{rs}_{2,hk} & v_l = 0, \\ 1 - q^{rs}_{2,hk} & v_l = 1. \end{cases} \tag{2.11}$$

pyr-to-pyr Two active pyramidal neurons do not directly influence each other in terms of deactivation. This reflects the nature of pyramidal-to-pyramidal connections, which are primarily excitatory and do not typically lead to direct inhibition in a single interaction. Then, for $r \in \{\hat{h}+1,\ \hat{h}+2, \ldots, n_h\}$ and $s \in \{\hat{k}+1,\ \hat{k}+2, \ldots, n_k\}$:

$$C^{rs}_{hk}(v_l, 1, 1) = \begin{cases} 0 & v_l = 0, \\ 1 & v_l = 1. \end{cases} \tag{2.12}$$

H6. The resting case corresponds to $(h, r) = (k, s)$ which represents self-interactions. A neuron in the microscopic state (h, r, v_n) cannot change its potential state v_n, meaning it does not interact with itself. Specifically, for all $h \in \{1, 2, \ldots, S\}$, $r \in \{1,\ 2, \ldots, \hat{h}-1,\ \hat{h},\ \hat{h}+1, \ldots, n_h\}$, and $v_n \in \{0,\ 1\}$:

$$C^{rr}_{hh}(v_l, v_n, v_n) = \begin{cases} 1 & v_l = v_n, \\ 0 & v_l \neq v_n. \end{cases} \tag{2.13}$$

Remark 1. *The above construction of the transition probability $C^{rs}_{hk}(v_l, v_n, v_m)$ models the level of inhibitory and excitatory activity of the overall network. In particular, the excitatory level is modulated by $p^{rs}_{1,hk}$ and $p^{rs}_{2,hk}$, whereas the inhibitory level is modulated by $q^{rs}_{1,hk}$ and $q^{rs}_{2,hk}$.*

Remark 2. *In general, the transition probability $C^{rs}_{hk}(v_l, v_n, v_m)$ is time-dependent to accurately model neuronal dynamics in a network. However, for the aim of this study, we assume it to be time-independent, and leave the investigation of time-dependent probabilities for future work.*

Remark 3. *As defined, the transition probability $C^{rs}_{hk}(v_l, v_n, v_m)$ may be such that*

$$C^{rs}_{hk}(v_{l_1}, v_n, v_m) \neq 0, \ v_{l_1} \neq v_n, \qquad C^{sr}_{kh}(v_{l_2}, v_m, v_n) = 0, \ v_{l_2} \neq v_n, \tag{2.14}$$

i.e., the neuron (h, r, v_n) can change its potential state due to the interaction with the neuron (k, s, v_m), but the reverse cannot occur. This property reflects the asymmetry and heterogeneity of the network. Specifically, the transition probability values $p^{rs}_{1,hk}$, $p^{rs}_{2,hk}$, $q^{rs}_{1,hk}$, and $q^{rs}_{2,hk}$ vary depending on the slices h, k, labels r, s, and the potential states v_n, v_m, v_l. This captures the network heterogeneity with respect to functional organization, i.e., interneurons and pyramidal neurons (see Figure 2).

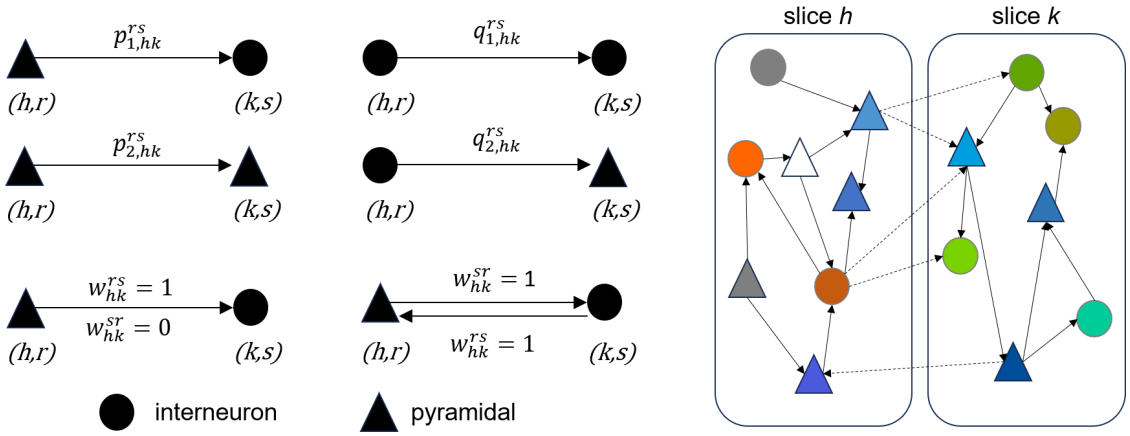

Figure 2. Heterogeneous network. The network heterogeneity with respect to both interneuron (circles) and pyramidal neuron (triangles) populations is highlighted through the transition probability values $p^{rs}_{1,hk}$, $p^{rs}_{2,hk}$, $q^{rs}_{1,hk}$, and $q^{rs}_{2,hk}$ (top, left) and the neuron distribution in each slice (colored circles and triangles on the right). The heterogeneous connectivity structure of the network is determined by the weights w^{rs}_{hk} (bottom, left) and is graphically represented by the arrows within (solid lines) and between (dashed lines) slices (right). All-to-all connectivity occurs when all weights w^{rs}_{hk} are non-zero.

Up to this point, we have provided a description that does not yet take into account the connectivity structure of the network. Typically, neuronal connectivity is defined by specific rules, ranging from random sparse to all-to-all connections. However, the brain comprises complex networks of interacting neurons that exhibit significant heterogeneity in both spiking dynamics and connectivity patterns. In particular, regions like the hippocampus display structured and directional connectivity, reflecting the functional specialization of neuronal populations [1, 52, 72]. These heterogeneous and anisotropic connection profiles critically shape neural dynamics and need to be incorporated into accurate network

models. To account for this, we introduce weights that describe the microscopic connectivity through some matrices. Therefore, for all $h, k \in \{1, 2, \dots, S\}$, $r \in \{1, 2, \dots, n_h\}$, and $s \in \{1, 2, \dots, n_k\}$, let $0 \le w_{hk}^{rs} \le 1$ be the *weight* that provides the connection between the neuron $(h,\ r)$ and the neuron $(k,\ s)$ (see Figure 2). For each pair of slices h and k, the weights w_{hk}^{rs} form a matrix also known in literature as an *adjacency matrix*. Specifically, an adjacency matrix is a matrix $A = (a_{ij})$ whose entry $a_{ij} \in \{0,\ 1\}$ encodes the presence of a connection from node i to node j in the network, i.e., $a_{ij} = 1$ [73]. More generally, a weight can be assigned to each connection, so that $a_{ij} \in [0, 1]$; in this case, one refers to a *weighted adjacency matrix* [40]. The latter is the type of structure adopted in the general framework considered in this study. Given the interpretation of the transition probabilities $C_{hk}^{rs}(v_l, v_n, v_m)$, the weight w_{hk}^{rs} models the connectivity from neuron $(k,\ s)$ to neuron (h, r). According to the graph theory, this quantity represents the connectivity structure of the network: if $w_{hk}^{rs} = 0$, the two neurons are not connected, at least in one direction (see Figure 2, bottom, left).

In order to derive the mesoscopic evolution from the microscopic description, we have to introduce mesoscopic quantities that incorporate the information provided by the transition probabilities, $C_{hk}^{rs}(v_l, v_n, v_m)$, and the connection weights, w_{hk}^{rs}. This latter component, associated with the weighted connectivity, represents the main novelty of the present framework compared to that proposed in [69]. Specifically, we introduce the following four quantities, which act as averages over each neuron type and each slice of the pointwise quantities previously introduced, for all $h, k \in \{1, 2, \dots, S\}$ and $l, n, m \in \{0,\ 1\}$:

$$
\begin{aligned}
D_{hk}^{\text{int-to-int}}(v_l, v_n, v_m) &:= \sum_{r=1}^{\hat{h}} \sum_{s=1}^{\hat{k}} w_{hk}^{rs} C_{hk}^{rs}(v_l, v_n, v_m), \\
D_{hk}^{\text{pyr-to-int}}(v_l, v_n, v_m) &:= \sum_{r=1}^{\hat{h}} \sum_{s=\hat{k}+1}^{n_k} w_{hk}^{rs}\, C_{hk}^{rs}(v_l, v_n, v_m), \\
D_{hk}^{\text{int-to-pyr}}(v_l, v_n, v_m) &:= \sum_{r=\hat{h}+1}^{n_h} \sum_{s=1}^{\hat{k}} w_{hk}^{rs}\, C_{hk}^{rs}(v_l, v_n, v_m), \\
D_{hk}^{\text{pyr-to-pyr}}(v_l, v_n, v_m) &:= \sum_{r=\hat{h}+1}^{n_h} \sum_{s=\hat{k}+1}^{n_k} w_{hk}^{rs}\, C_{hk}^{rs}(v_l, v_n, v_m).
\end{aligned}
\tag{2.15}
$$

The above quantities (2.15) can be interpreted as averages of transition probabilities, $C_{hk}^{rs}(v_l, v_n, v_m)$, over the network, weighted by w_{hk}^{rs}, for each slice and for each type of binary interaction. Due to the assumption (2.1), one has

$$
\begin{aligned}
&\sum_{l=0}^{1} D_{hk}^{\text{int-to-int}}(v_l, v_n, v_m) = \sum_{r=1}^{\hat{h}} \sum_{s=1}^{\hat{k}} w_{hk}^{rs}, \qquad \sum_{l=0}^{1} D_{hk}^{\text{pyr-to-int}}(v_l, v_n, v_m) = \sum_{r=1}^{\hat{h}} \sum_{s=\hat{k}+1}^{n_k} w_{hk}^{rs}, \\
&\sum_{l=0}^{1} D_{hk}^{\text{int-to-pyr}}(v_l, v_n, v_m) = \sum_{r=\hat{h}+1}^{n_h} \sum_{s=1}^{\hat{k}} w_{hk}^{rs}, \quad \sum_{l=0}^{1} D_{hk}^{\text{pyr-to-pyr}}(v_l, v_n, v_m) = \sum_{r=\hat{h}+1}^{n_h} \sum_{s=\hat{k}+1}^{n_k} w_{hk}^{rs}.
\end{aligned}
\tag{2.16}
$$

The modeling choices at the microscopic level ensure that the neuronal network remains inherently heterogeneous in its functionality, and both anisotropic and heterogeneous in its connectivity structure. Specifically, the network is partitioned into S slices, each containing both interneurons and pyramidal

neurons. These neurons are interconnected through the weights w_{hk}^{rs}, which shape the connectivity in different ways and, along with the transition probabilities $C_{hk}^{rs}(v_l, v_n, v_m)$, determine the evolution of the network.

In order to describe the mesoscopic evolution of the system, we introduce the following two *distribution functions*:

$$N_{h,\mathrm{int}}(t, v_l) : [0,\ T] \times \{0,\ 1\} \to \mathbb{R}^+, \quad N_{h,\mathrm{pyr}}(t, v_l) : [0,\ T] \times \{0,\ 1\} \to \mathbb{R}^+,$$

which represent the number of interneurons and pyramidal neurons in the slice h with potential v_l, at time $t > 0$, for $h \in \{1, 2, \ldots, S\}$ and $l \in \{0,\ 1\}$, respectively.

Specifically, $N_{h,\mathrm{int}}(t, 0)$ and $N_{h,\mathrm{int}}(t, 1)$ denote the total number of inactive and active interneurons of the hth slice at time $t > 0$, respectively. Similarly, $N_{h,\mathrm{pyr}}(t, 0)$ and $N_{h,\mathrm{pyr}}(t, 1)$ represent the active and inactive pyramidal neurons, respectively. Therefore, the total number of interneurons and pyramidal neurons in the whole network with potential v_l at time $t > 0$, for $l \in \{0, 1\}$, is given by the following quantities:

$$N_{\mathrm{int}}(t, v_l) := \sum_{h=1}^{S} N_h^{\mathrm{int}}(t, v_l), \quad N_{\mathrm{pyr}}(t, v_l) := \sum_{h=1}^{S} N_h^{\mathrm{pyr}}(t, v_l).$$

Finally, the overall number of neurons is

$$N := \sum_{h=1}^{S} \sum_{l=0}^{1} \Big[N_{h,\mathrm{int}}(t,\ v_l) + N_{h,\mathrm{pyr}}(t,\ v_l) \Big], \qquad \forall t \geq 0.$$

Then, integrating the additional parameters introduced above, and assuming spatial homogeneity within each slice in accordance with the adopted modeling framework, at the mesoscopic level, the *discrete kinetic model* that describes the evolution of interneurons and pyramidal neurons, respectively, in slice h, with potential v_l, for $h \in \{1, 2, \ldots, S\}$ and $l \in \{0, 1\}$, is [53, 69]

$$\begin{aligned} \frac{d}{dt} N_{h,\mathrm{int}}(t, v_l) = & \sum_{k=1}^{S} \sum_{n,m=0}^{1} D_{hk}^{\text{int-to-int}}(v_l, v_n, v_m) N_{h,\mathrm{int}}(t, v_n) N_{k,\mathrm{int}}(t, v_m) \\ & + \sum_{k=1}^{S} \sum_{n,m=0}^{1} D_{hk}^{\text{pyr-to-int}}(v_l, v_n, v_m) N_{h,\mathrm{int}}(t, v_n) N_{k,\mathrm{pyr}}(t, v_m) \\ & - \sum_{k=1}^{S} \sum_{m=0}^{1} \Bigg[\sum_{r=1}^{\hat{h}} \sum_{s=1}^{\hat{k}} w_{hk}^{rs} N_{h,\mathrm{int}}(t, v_l) N_{k,\mathrm{int}}(t, v_m) \\ & \qquad + \sum_{r=1}^{\hat{h}} \sum_{s=\hat{k}+1}^{n_k} w_{hk}^{rs} N_{h,\mathrm{int}}(t, v_l) N_{k,\mathrm{pyr}}(t, v_m) \Bigg], \end{aligned} \tag{2.17}$$

$$\begin{aligned}\frac{d}{dt}N_{h,\mathrm{pyr}}(t,v_l) &= \sum_{k=1}^{S}\sum_{n,m=0}^{1} D_{hk}^{\text{int-to-pyr}}(v_l,v_n,v_m)N_{h,\mathrm{pyr}}(t,v_n)N_{k,\mathrm{int}}(t,v_m)\\ &+ \sum_{k=1}^{S}\sum_{n,m=0}^{1} D_{hk}^{\text{pyr-to-pyr}}(v_l,v_n,v_m)N_{h,\mathrm{pyr}}(t,v_n)N_{k,\mathrm{pyr}}(t,v_m)\\ &- \sum_{k=1}^{S}\sum_{m=0}^{1}\Bigg[\sum_{r=\hat{h}+1}^{n_h}\sum_{s=1}^{\hat{k}} w_{hk}^{rs}N_{h,\mathrm{pyr}}(t,v_l)N_{k,\mathrm{int}}(t,v_m)\\ &\qquad + \sum_{r=\hat{h}+1}^{n_h}\sum_{s=\hat{k}+1}^{n_k} w_{hk}^{rs}N_{h,\mathrm{pyr}}(t,v_l)N_{k,\mathrm{pyr}}(t,v_m)\Bigg].\end{aligned} \tag{2.18}$$

Equation (2.17) describes the evolution of the number of interneurons in slice h with potential v_l, denoted as $N_{h,\mathrm{int}}(t,v_l)$. In particular, the first two terms on the right-hand side represent the number of interneurons that acquire the potential v_l due to binary interaction with other neurons. Conversely, the third term represents the number of interneurons that lose the potential v_l due to binary interaction. The same reasoning applies to pyramidal neurons. Notably, for $v_l = 1$, the kinetic equations provide the evolution of active neurons, whereas for $v_l = 0$, they describe the evolution of inactive neurons.

The model described in Eqs (2.17) and (2.18) is a system of nonlinear ordinary differential equations, with quadratic nonlinearity. The positive initial data $\mathbf{N}_0$ to be assigned to the systems (2.17) and (2.18) is

$$\mathbf{N}_0 = \Big[N_{h,\mathrm{int},0}(v_l),\ N_{h,\mathrm{pyr},0}(v_l)\Big]_{\substack{h\in\{1,2,\dots,S\}\\ l\in\{0,1\}}}.$$

In particular, $N_{h,\mathrm{int},0}(0)$ and $N_{h,\mathrm{int},0}(1)$ represent the total number of inactive and active interneurons, respectively, at the initial time $t = 0$; whereas, $N_{h,\mathrm{pyr},0}(0)$ and $N_{h,\mathrm{pyr},0}(1)$ play the same role for pyramidal neurons. Then, $N_{h,0}^{\mathrm{int}}(1) + N_{h,0}^{\mathrm{pyr}}(1)$ is the total number of active neurons in the network at the initial time, whereas $N_{h,0}^{\mathrm{int}}(0) + N_{h,0}^{\mathrm{pyr}}(0)$ is the total number of inactive neurons at the initial time. Moreover,

$$\sum_{h=1}^{S}\sum_{l=0}^{1} N_{h,\mathrm{int},0}(v_l) + \sum_{h=1}^{S}\sum_{l=0}^{1} N_{h,\mathrm{pyr},0}(v_l) = N,$$

and, for all $h \in \{1,2,\dots,S\}$,

$$n_{h,\mathrm{int}} = \hat{h} = N_{h,\mathrm{int},0}(0) + N_{h,\mathrm{int},0}(1), \quad n_{h,\mathrm{pyr}} = n_h - \hat{h} = N_{h,\mathrm{pyr},0}(0) + N_{h,\mathrm{pyr},0}(1). \tag{2.19}$$

Therefore, once the initial data $\mathbf{N}_0$ is assigned, the *initial value problem* related to the kinetic systems (2.17) and (2.18) is well-defined, according to the arguments provided in [69]. Indeed, let us consider a positive initial condition $\mathbf{N}_0$, as stated above. As all coefficients of kinetic equations (2.17) and (2.18) are constant in time, along with assumption **H1**, the right-hand side of the systems (2.17) and (2.18) is C^1 (see for further details, for instance, [69]), and then locally Lipschitz continuous. Therefore, by the Picard–Lindelöf theorem, the initial value problem admits a unique solution $\mathbf{N}(t)$. Moreover, the positivity of the initial data guarantees that the solution $\mathbf{N}(t)$ remains positive for all t. Indeed, systems (2.17) and (2.18) can be written as

$$\begin{aligned}\frac{d}{dt}N_{h,\mathrm{int}}(t,v_l) &= \Gamma_{h,\mathrm{int}}(t,v_l) - N_{h,\mathrm{int}}(t,v_l)\Theta_{h,\mathrm{int}}(t),\\ \frac{d}{dt}N_{h,\mathrm{pyr}}(t,v_l) &= \Gamma_{h,\mathrm{pyr}}(t,v_l) - N_{h,\mathrm{pyr}}(t,v_l)\Theta_{h,\mathrm{pyr}}(t),\end{aligned} \tag{2.20}$$

where

$$\begin{aligned}
\Gamma_{h,\mathrm{int}}(t,v_l) &:= \sum_{k=1}^{S}\sum_{n,m=0}^{1} D_{hk}^{\text{int-to-int}}(v_l,v_n,v_m)N_{h,\mathrm{int}}(t,v_n)N_{k,\mathrm{int}}(t,v_m)\\
&\quad+\sum_{k=1}^{S}\sum_{n,m=0}^{1} D_{hk}^{\text{pyr-to-int}}(v_l,v_n,v_m)N_{h,\mathrm{int}}(t,v_n)N_{k,\mathrm{pyr}}(t,v_m),\\
\Theta_{h,\mathrm{int}}(t) &:= \sum_{k=1}^{S}\sum_{m=0}^{1}\left[\sum_{r=1}^{\hat{h}}\sum_{s=1}^{\hat{k}} w_{hk}^{rs}N_{k,\mathrm{int}}(t,v_m)+\sum_{r=1}^{\hat{h}}\sum_{s=\hat{k}+1}^{n_k} w_{hk}^{rs}N_{k,\mathrm{pyr}}(t,v_m)\right],
\end{aligned}\tag{2.21}$$

$$\begin{aligned}
\Gamma_{h,\mathrm{pyr}}(t,v_l) &:= \sum_{k=1}^{S}\sum_{n,m=0}^{1} D_{hk}^{\text{int-to-pyr}}(v_l,v_n,v_m)N_{h,\mathrm{pyr}}(t,v_n)N_{k,\mathrm{int}}(t,v_m)\\
&\quad+\sum_{k=1}^{S}\sum_{n,m=0}^{1} D_{hk}^{\text{pyr-to-pyr}}(v_l,v_n,v_m)N_{h,\mathrm{pyr}}(t,v_n)N_{k,\mathrm{pyr}}(t,v_m),\\
\Theta_{h,\mathrm{pyr}}(t) &:= \sum_{k=1}^{S}\sum_{m=0}^{1}\left[\sum_{r=\hat{h}+1}^{n_h}\sum_{s=1}^{\hat{k}} w_{hk}^{rs}N_{k,\mathrm{int}}(t,v_m)+\sum_{r=\hat{h}+1}^{n_h}\sum_{s=\hat{k}+1}^{n_k} w_{hk}^{rs}N_{k,\mathrm{pyr}}(t,v_m)\right].
\end{aligned}\tag{2.22}$$

Due to the positivity of transition probabilities and adjacency matrices, we have that

$$\Gamma_{h,\mathrm{int}}(t,v_l),\ \Gamma_{h,\mathrm{pyr}}(t,v_l),\ \Theta_{h,\mathrm{int}}(t),\ \Theta_{h,\mathrm{pyr}}(t)\geq 0.$$

Straightforward calculations show that system (2.20) becomes

$$\begin{aligned}
N_{h,\mathrm{int}}(t,v_l) &= e^{-\int_0^t \Theta_{h,\mathrm{int}}(s)\,ds}\left[N_{h,\mathrm{int},0}(v_l)+\int_0^t \Gamma_{h,\mathrm{int}}(s,v_l)\,e^{\int_0^s \Theta_{h,\mathrm{int}}(\tau)\,d\tau}\,ds\right],\\
N_{h,\mathrm{pyr}}(t,v_l) &= e^{-\int_0^t \Theta_{h,\mathrm{pyr}}(s)\,ds}\left[N_{h,\mathrm{pyr},0}(v_l)+\int_0^t \Gamma_{h,\mathrm{pyr}}(s,v_l)\,e^{\int_0^s \Theta_{h,\mathrm{pyr}}(\tau)\,d\tau}\,ds\right],
\end{aligned}\tag{2.23}$$

which ensures that the solution remains positive.

In particular, the total number of neurons, both active and inactive, is conserved within each slice. Therefore, by using the kinetic framework (2.17) and (2.18) along with the assumption **H1**, it follows that for all $h\in\{1,2,\dots,S\}$ and for all $t\geq 0$,

$$\sum_{l=0}^{1} N_{h,\mathrm{int}}(t,\ v_l)=N_{h,\mathrm{int},0}(0)+N_{h,\mathrm{int},0}(1),\qquad \sum_{l=0}^{1} N_{h,\mathrm{pyr}}(t,\ v_l)=N_{h,\mathrm{pyr},0}(0)+N_{h,\mathrm{pyr},0}(1).\tag{2.24}$$

Finally, the global-in-time existence of the solution could fail only if $|N_{h,\mathrm{int}}|\to+\infty$ and/or $|N_{h,\mathrm{pyr}}|\to+\infty$ as $t\to\hat{t}$ for some $\hat{t}<+\infty$. However, for the solution here obtained, this eventuality is excluded by Eq (2.24). Therefore, there exists a unique positive solution $\mathbf{N}(t)$, global in time, which preserves the total number of the involved neurons.

Recall that $n_{h,\text{int}}$ and $n_{h,\text{pyr}}$ represent the total number of interneurons and pyramidal neurons, respectively, in the slice h. Then, by using the conservation law Eq (2.24), one has the following first integral for each slice h, for $h \in \{1, 2, \dots, S\}$,

$$N_{h,\text{int}}(t, 0) = n_{h,\text{int}} - N_{h,\text{int}}(t, 1), \qquad N_{h,\text{pyr}}(t, 0) = n_{h,\text{pyr}} - N_{h,\text{pyr}}(t, 1). \tag{2.25}$$

Therefore, solving the initial value problem associated with Eqs (2.17) and (2.18), even from a numerical perspective, requires solving only half of the $2 \times 2 \times S$ ordinary differential equations. Specifically, the system can be solved with respect to, for instance, active interneurons and pyramidal neurons, i.e., for $v_l = 1$. It is worth noting that the condition (2.25) allows the entire system to be written in closed form as a function of $N_h^{\text{int}}(t, 1)$ and $N_h^{\text{pyr}}(t, 1)$.

3. Simplified network model with slice-specific heterogeneity in connectivity and transition probabilities

This section is devoted to a specialization of the kinetic models (2.17) and (2.18) focusing on a network comprising multiple slices, under simplified assumptions regarding both the connectivity structure and transition probabilities (see Figure 3). Specifically, we consider S interacting slices composed of $n_{h,\text{int}}$ interneurons and $n_{h,\text{pyr}}$ pyramidal neurons, for $h = 1, \dots, S$, and assume that the interactions between pairs of neurons depend solely on their type (interneurons or pyramidal neurons) and the slice to which they belong. Therefore, the adjacency matrices, $w_{hk}^{rs} \in \{0, 1\}$, and the transition probabilities, $C_{hk}^{rs}(v_l, v_n, v_m)$, depend only on whether the neurons belong to the same slice or not, which allows us to simplify the notation of the parameters involved in the system with respect to the more general framework introduced in the previous section. It is worth emphasizing that the discrete kinetic systems (2.17) and (2.18) can be applied to a network of neurons, each characterized by its own functionality and spatial properties. When $h = k$ we refer to *within-group interactions*, while for $h \neq k$, we refer to *between-group interactions*. For the former, we will use the superscript w, while for the latter, b. Assuming that only a fraction of neurons are connected, we consider that $\alpha^{w_h}, \beta^{w_h}, \gamma^{w_h}, \delta^{w_h}$, for $h \in \{1, .., S\}$, refer to within-group connections (i.e., w_{hh}^{rs}), while $\alpha^{b_{hk}}, \beta^{b_{hk}}, \gamma^{b_{hk}}, \delta^{b_{hk}}$, for $h, k \in \{1, .., S\}$ with $h \neq k$, refer to between-group connections (i.e., w_{hk}^{rs}) as follows:

$$\begin{aligned}
&\sum_{r,s=1}^{n_{h,\text{int}}} w_{hh}^{rs} = \alpha^{w_h} n_{h,\text{int}}^2, \qquad \sum_{r,s=1}^{n_{h,\text{pyr}}} w_{hh}^{rs} = \beta^{w_h} n_{h,\text{pyr}}^2,\\
&\sum_{r=1}^{n_{h,\text{pyr}}} \sum_{s=1}^{n_{h,\text{int}}} w_{hh}^{rs} = \delta^{w_h} n_{h,\text{pyr}} n_{h,\text{int}}, \quad \sum_{r=1}^{n_{h,\text{int}}} \sum_{s=1}^{n_{h,\text{pyr}}} w_{hh}^{rs} = \gamma^{w_h} n_{h,\text{int}} n_{h,\text{pyr}},\\
&\sum_{r=1}^{n_{h,\text{int}}} \sum_{s=1}^{n_{k,\text{int}}} w_{hk}^{rs} = \alpha^{b_{kh}} n_{h,\text{int}} n_{k,\text{int}}, \quad \sum_{r=1}^{n_{h,\text{pyr}}} \sum_{s=1}^{n_{k,\text{pyr}}} w_{hk}^{rs} = \beta^{b_{kh}} n_{h,\text{pyr}} n_{k,\text{pyr}},\\
&\sum_{r=1}^{n_{h,\text{pyr}}} \sum_{s=1}^{n_{k,\text{int}}} w_{hk}^{rs} = \delta^{b_{kh}} n_{h,\text{pyr}} n_{k,\text{int}}, \quad \sum_{r=1}^{n_{h,\text{int}}} \sum_{s=1}^{n_{k,\text{pyr}}} w_{hk}^{rs} = \gamma^{b_{kh}} n_{h,\text{int}} n_{k,\text{pyr}}.
\end{aligned} \tag{3.1}$$

In particular, for each slice $h \in \{1, \dots, S\}$, the coefficients $\alpha^{w_h}, \beta^{w_h}, \gamma^{w_h}, \delta^{w_h}$ denote the fractions of connections within the same slice, corresponding respectively to interneuron-to-interneuron, pyramidal-to-pyramidal, pyramidal-to-interneuron, and interneuron-to-pyramidal connections. Analogously, for

$h, k \in \{1, \ldots, S\}$ with $h \neq k$, the coefficients $\alpha^{b_{hk}}, \beta^{b_{hk}}, \gamma^{b_{hk}}, \delta^{b_{hk}}$ represent the corresponding fractions of connections between neurons belonging to different slices (Figure 3, left panel). Furthermore, *homogeneous connectivity* arises if and only if

$$\alpha^{w_h} = \alpha^{b_{hk}} = \alpha, \quad \beta^{w_h} = \beta^{b_{hk}} = \beta, \quad \gamma^{w_h} = \gamma^{b_{hk}} = \gamma, \quad \delta^{w_h} = \delta^{b_{hk}} = \delta, \qquad \forall h,\ k \neq h, \tag{3.2}$$

whereas *all-to-all connectivity* occurs when $\alpha = \beta = \gamma = \delta = 1$. Similarly, the transition probabilities are determined based on whether the interactions occur between neurons (interneurons or pyramidal neurons) within the same slice (i.e., $p_1^{w_h}, p_2^{w_h}, q_1^{w_h}, q_2^{w_h}$) or across different slices (i.e., $p_1^{b_{hk}}, p_2^{b_{hk}}, q_1^{b_{hk}}, q_2^{b_{hk}}$), introducing functional heterogeneity only between slices (see Figure 3, right panel). Likewise, *functional homogeneity* arises if and only if

$$p_1^{w_h} = p_1^{b_{hk}} = p_1, \quad p_2^{w_h} = p_2^{b_{hk}} = p_2, \quad q_1^{w_h} = q_1^{b_{hk}} = q_1, \quad q_2^{w_h} = q_2^{b_{hk}} = q_2, \qquad \forall h,\ k \neq h, \tag{3.3}$$

whereas heterogeneity in the proportions of excitatory and inhibitory neurons across slices and throughout the network is explicitly encoded in the network structure via the total number of interneurons ($n_{h,\text{int}}$) and pyramidal neurons ($n_{h,\text{pyr}}$) in each slice.

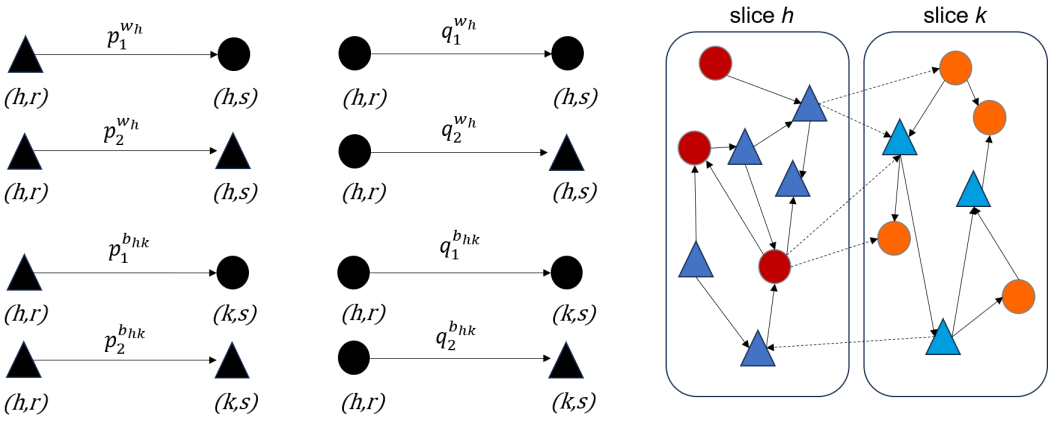

Figure 3. Simplified network model with slice-specific heterogeneity. When neurons within the same slice interact, the transition probabilities $p_1^{w_h}, p_2^{w_h}, q_1^{w_h}, q_2^{w_h}$ remain homogeneous for each interaction type (pyr-to-int, pyr-to-pyr, int-to-int, and int-to-pyr) (top left). When the interacting neurons belong to different slices, these probabilities may vary ($p_1^{b_{hk}}, p_2^{b_{hk}}, q_1^{b_{hk}}, q_2^{b_{hk}}$, bottom left). The heterogeneous connectivity structure of the network is defined by the fractions $\alpha^{w_h}, \beta^{w_h}, \gamma^{w_h}, \delta^{w_h}$ (within-slice) and $\alpha^{b_{hk}}, \beta^{b_{hk}}, \gamma^{b_{hk}}, \delta^{b_{hk}}$ (between-slice), represented by solid and dashed lines (right). Variations in the relative numbers of excitatory and inhibitory neurons across slices are captured by the total number of interneurons ($n_{h,\text{int}}$) and pyramidal neurons ($n_{h,\text{pyr}}$) in each slice.

In view of the first integrals (2.25), the kinetic systems (2.17) and (2.18), under the assumptions of

this section, can be written as follows:

$$\begin{aligned}
\frac{d}{dt}N_{h,\mathrm{int}}(1) = &- \sum_{k=1,k\neq h}^{S} \alpha^{b_{kh}} q_1^{b_{kh}} n_{h,\mathrm{int}} n_{k,\mathrm{int}} N_{h,\mathrm{int}}(1) N_{k,\mathrm{int}}(1) - \alpha^{w_h} q_1^{w_h} n_{h,\mathrm{int}}^2 N_{h,\mathrm{int}}^2(1) \\
&+ \sum_{k=1,k\neq h}^{S} \gamma^{b_{kh}} p_1^{b_{kh}} n_{k,\mathrm{pyr}} n_{h,\mathrm{int}} N_{h,\mathrm{int}}(0) N_{k,\mathrm{pyr}}(1) + \gamma^{w_h} p_1^{w_h} n_{h,\mathrm{pyr}} n_{h,\mathrm{int}} N_{h,\mathrm{int}}(0) N_{h,\mathrm{pyr}}(1), \\
\frac{d}{dt}N_{h,\mathrm{pyr}}(1) = &- \sum_{k=1,k\neq h}^{S} \delta^{b_{kh}} q_2^{b_{kh}} n_{k,\mathrm{int}} n_{h,\mathrm{pyr}} N_{h,\mathrm{pyr}}(1) N_{k,\mathrm{int}}(1) - \delta^{w_h} q_2^{w_h} n_{h,\mathrm{int}} n_{h,\mathrm{pyr}} N_{h,\mathrm{pyr}}(1) N_{h,\mathrm{int}}(1) \\
&+ \sum_{k=1,k\neq h}^{S} \beta^{b_{kh}} p_2^{b_{kh}} n_{h,\mathrm{pyr}} n_{k,\mathrm{pyr}} N_{h,\mathrm{pyr}}(0) N_{k,\mathrm{pyr}}(1) + \beta^{w_h} p_2^{w_h} n_{h,\mathrm{pyr}}^2 N_{h,\mathrm{pyr}}(0) N_{h,\mathrm{pyr}}(1),
\end{aligned} \tag{3.4}$$

for each slice h, for $h \in \{1, 2, \ldots, S\}$.

Furthermore, for any initial condition, the Cauchy problem associated with system (3.4) is well-defined and admits a unique global solution.

The dynamics of active interneurons are modulated by the network interactions: *inhibitory rates* $\gamma^{b_{kh}} p_1^{b_{kh}} n_{k,\mathrm{pyr}} n_{h,\mathrm{int}}$ and $\gamma^{w_h} p_1^{w_h} n_{h,\mathrm{pyr}} n_{h,\mathrm{int}}$ promote activation, whereas *excitatory rates* $\alpha^{b_{kh}} q_1^{b_{kh}} n_{h,\mathrm{int}} n_{k,\mathrm{int}}$ and $\alpha^{w_h} q_1^{w_h} n_{h,\mathrm{int}}^2$ lead to deactivation. Similarly, the dynamics of active pyramidal neurons are governed by the network interactions, where the *excitatory rates* $p_2^{b_{kh}} n_{h,\mathrm{pyr}} n_{k,\mathrm{pyr}}$ and $\beta^{w_h} p_2^{w_h} n_{h,\mathrm{pyr}}^2$ enhance activation, while the *inhibitory rates* $\delta^{b_{kh}} q_2^{b_{kh}} n_{k,\mathrm{int}} n_{h,\mathrm{pyr}}$ and $\delta^{w_h} q_2^{w_h} n_{h,\mathrm{int}} n_{h,\mathrm{pyr}}$ reduce it. In this framework, a network is said to operate in an *inhibitory-count-dominated* or *excitatory-count-dominated* regime when inhibitory (interneurons) or excitatory (pyramidal) neurons, respectively, constitute the larger fraction of active neurons over a given time interval. Numerical results suggest how to determine a priori whether the network operates in an inhibitory-count-dominated or excitatory-count-dominated regime, based on the relative magnitudes of the following overall inhibition-count and excitation-count rates

$$\begin{aligned}
\Phi_E := &\left[\sum_{h=1}^{S} \Big(\sum_{\substack{k=1 \\ k\neq h}}^{S} \alpha^{b_{kh}} q_1^{b_{kh}} n_{h,\mathrm{int}} n_{k,\mathrm{int}} + \alpha^{w_h} q_1^{w_h} n_{h,\mathrm{int}}^2 \Big) \right] \\
&\times \left[\sum_{h=1}^{S} \Big(\sum_{\substack{k=1 \\ k\neq h}}^{S} \beta^{b_{kh}} p_2^{b_{kh}} n_{h,\mathrm{pyr}} n_{k,\mathrm{pyr}} + \beta^{w_h} p_2^{w_h} n_{h,\mathrm{pyr}}^2 \Big) \right], \\
\Phi_I := &\left[\sum_{h=1}^{S} \Big(\sum_{\substack{k=1 \\ k\neq h}}^{S} \delta^{b_{kh}} q_2^{b_{kh}} n_{k,\mathrm{int}} n_{h,\mathrm{pyr}} + \delta^{w_h} q_2^{w_h} n_{h,\mathrm{int}} n_{h,\mathrm{pyr}} \Big) \right] \\
&\times \left[\sum_{h=1}^{S} \Big(\sum_{\substack{k=1 \\ k\neq h}}^{S} \gamma^{b_{kh}} p_1^{b_{kh}} n_{k,\mathrm{pyr}} n_{h,\mathrm{int}} + \gamma^{w_h} p_1^{w_h} n_{h,\mathrm{pyr}} n_{h,\mathrm{int}} \Big) \right].
\end{aligned} \tag{3.5}$$

In detail, we obtain the results summarized in Table 1. It can be easily observed that heterogeneous connections, or functional heterogeneity among neuron populations, can shift a network from an excitatory-count-dominated to an inhibitory-count-dominated regime, or vice versa.

In the following, we analyze the simplified network model in the cases $S = 1$, $S = 2$, and $S = 4$. Specifically, for $S = 1$, we consider the entire network, where the transition probabilities remain homogeneous for each interaction type (pyr-to-pyr, int-to-pyr, pyr-to-int, and int-to-int), while the connectivity structure remains heterogeneous according to Eq (3.1). In this case, a stability analysis identifies, in all cases, the presence of a locally asymptotically stable coexistence equilibrium. This result allows us to conclude that the presence of homogeneous transition probabilities ensures that the network remains active if it was initially active, and, over a long period, this activity is characterized by a constant number of active interneurons and pyramidal neurons. In this case, the results reported in Table 1 are analytically demonstrated. When $S = 2$, we analyze a network with two interacting slices, where the transition probabilities remain homogeneous for each type of interaction (pyr-to-pyr, int-to-pyr, pyr-to-int, and int-to-int), but they may vary when the interacting neurons belong to different slices. In particular, we examine the local dynamics of the slices when the overall dynamics of the network can also be effectively described using the one-slice model. Finally, we perform some interesting numerical simulations for $S = 1, 2, 4$, highlighting differences and similarities in the network dynamics with respect to different levels of heterogeneity in terms of transition probabilities and connectivity structure.

Table 1. Network regimes are determined by the balance between the excitatory-count rate Φ_E and the inhibitory-count rate Φ_I.

Condition	Network regime
$\Phi_E > \Phi_I$	excitation-count-dominated
$\Phi_E < \Phi_I$	inhibition-count-dominated
$\Phi_E = \Phi_I$	balanced count

3.1. One-slice model

In this section, we specialize the kinetic model to the entire network, i.e., $S = 1$. Therefore, system (3.4) can be written in the following form:

$$\begin{aligned} \frac{d}{dt}N_{\text{int}}(1) &= -q_1\alpha n_{\text{int}}^2 N_{\text{int}}^2(1) + p_1\gamma\, n_{\text{int}} n_{\text{pyr}} N_{\text{pyr}}(1) N_{\text{int}}(0), \\ \frac{d}{dt}N_{\text{pyr}}(1) &= -q_2\delta n_{\text{pyr}} n_{\text{int}} N_{\text{pyr}}(1) N_{\text{int}}(1) + p_2\beta n_{\text{pyr}}^2 N_{\text{pyr}}(1) N_{\text{pyr}}(0), \end{aligned} \tag{3.6}$$

where n_{int} and n_{pyr} represent the total number of interneurons and pyramidal neurons in the network, respectively. The adjacency matrices are given by

$$\sum_{r,s=1}^{n_{\text{int}}} w^{rs} = \alpha\, n_{\text{int}}^2, \quad \sum_{r,s=1}^{n_{\text{pyr}}} w^{rs} = \beta\, n_{\text{pyr}}^2, \quad \sum_{r=1}^{n_{\text{int}}}\sum_{s=1}^{n_{\text{pyr}}} w^{rs} = \gamma\, n_{\text{int}} n_{\text{pyr}}, \quad \sum_{r=1}^{n_{\text{pyr}}}\sum_{s=1}^{n_{\text{int}}} w^{rs} = \delta\, n_{\text{pyr}} n_{\text{int}}, \tag{3.7}$$

and the transition probabilities $p_1,\ p_2,\ q_1,\ q_2$ refer to the homogeneous interactions of pyr-to-int, pyr-to-pyr, int-to-int, and int-to-pyr type, respectively. System (3.6) is not in closed form, allowing a clear identification of pairwise interactions between neurons of the same or different types. The contributions of the four terms in the differential equations can be explicitly distinguished: $(q_1\alpha\, n_{\text{int}}^2,\ p_2\beta\, n_{\text{pyr}}^2)$ govern excitation, forming the excitatory-count rate Φ_E, while $(p_1\gamma\, n_{\text{int}} n_{\text{pyr}},\ q_2\delta\, n_{\text{pyr}} n_{\text{int}})$ govern inhibition, forming the inhibitory-count rate Φ_I (see Eq (3.5)). When both Φ_E and Φ_I are nonzero, the ratio

Φ_E/Φ_I does not depend on n_{int} or n_{pyr}, and the network operates in an inhibitory-count-dominated or excitatory-count-dominated regime when $\Phi_E/\Phi_I < 1$ or $\Phi_E/\Phi_I > 1$, respectively. These results can be analytically verified via a stability analysis of the system, together with the case in which $\Phi_E = \Phi_I$, when the network is count-balanced, as will be done in the following part of this section. For now, it is worth examining the limiting cases in which $\Phi_E = 0$ or $\Phi_I = 0$. In detail, we obtain:

- For $p_1\gamma = 0$ or $q_2\delta = 0$, i.e., $\Phi_I = 0$, system (3.6) becomes decoupled, since interneurons do not interact with pyramidal neurons or vice versa. This results in logistic growth for the active pyramidal neurons and an exponential decay to zero for the interneurons, respectively.
- For $p_2\beta = 0$ or $q_1\alpha = 0$, i.e., $\Phi_E = 0$, the dynamics of pyramidal neurons are no longer sustained by mutual activation, so their number can only decrease due to the action of active interneurons, while interneurons, in the absence of self-inhibition, can only be activated by pyramidal neurons.

To perform the stability analysis, we consider the following closed form of system (3.4):

$$\begin{aligned}
\frac{d}{dt}N_{\text{int}}(1) &= -q_1\alpha n_{\text{int}}^2 N_{\text{int}}^2(1) + p_1\gamma\, n_{\text{int}}^2 n_{\text{pyr}} N_{\text{pyr}}(1) - p_1\gamma n_{\text{int}} n_{\text{pyr}} N_{\text{int}}(1) N_{\text{pyr}}(1),\\
\frac{d}{dt}N_{\text{pyr}}(1) &= -q_2\delta n_{\text{pyr}} n_{\text{int}} N_{\text{pyr}}(1) N_{\text{int}}(1) + p_2\beta n_{\text{pyr}}^3 N_{\text{pyr}}(1) - p_2\beta n_{\text{pyr}}^2 N_{\text{pyr}}^2(1).
\end{aligned} \tag{3.8}$$

We introduce the following dimensionless variables:

$$\tilde{N}_{\text{int}}(1) = \frac{N_{1,\text{int}}(1)}{\Omega}, \quad \tilde{N}_{\text{pyr}}(1) = \frac{N_{1,\text{pyr}}(1)}{\Psi}, \quad \tilde{t}_{\text{int}} = \frac{t}{\tau}, \quad \tilde{t}_{\text{pyr}} = \frac{t}{\Gamma}, \tag{3.9}$$

where

$$\Omega = n_{\text{int}}, \quad \Psi = n_{\text{pyr}}, \quad \tau = \frac{1}{n_{\text{int}} n_{\text{pyr}}^2 p_1\gamma}, \quad \Gamma = \frac{1}{n_{\text{pyr}}^3 p_2\beta}. \tag{3.10}$$

Equation (3.8) becomes

$$\begin{aligned}
\frac{d}{dt_{\text{int}}}N_{\text{int}}(1) &= -LN_{\text{int}}^2(1) + N_{\text{pyr}}(1) - N_{\text{int}}(1)N_{\text{pyr}}(1),\\
\frac{d}{dt_{\text{pyr}}}N_{\text{pyr}}(1) &= N_{\text{pyr}}(1) - HN_{\text{int}}(1)N_{\text{pyr}}(1) - N_{\text{pyr}}^2(1),
\end{aligned} \tag{3.11}$$

with

$$L = \frac{n_{\text{int}}^2 q_1\alpha}{n_{\text{pyr}}^2 p_1\gamma}, \quad H = \frac{n_{\text{int}}^2 q_2\delta}{n_{\text{pyr}}^2 p_2\beta}, \tag{3.12}$$

where, for simplicity, we omitted the tildes.

We remark that $L/H = \Phi_E/\Phi_I$. Furthermore, since system (3.11) describes the dynamics of the fractions of active interneurons and pyramidal neurons, the ensuing stability analysis can be directly used to rigorously establish the results reported in Table 1.

System (3.11) always admits the trivial equilibrium $E_0 = (0, 0)$, whereas it exhibits three positive coexistence equilibrium configurations $E_i = (N_{\text{int},i}^*, N_{\text{pyr},i}^*)$, $i = 1, 2, 3$, whose existence depends on the relative magnitudes of the parameters L and H as follows:

- For $H > 0$ and $0 < L < H$, i.e., $\Phi_E/\Phi_I < 1$,

$$E_1 = \left(\frac{1}{2}\left(\frac{H+1}{H-L} - \sqrt{\frac{(H-1)^2+4L}{(H-L)^2}}\right), \frac{1}{2}\left(2 + \frac{H(H+1)}{L-H} + H\sqrt{\frac{(H-1)^2+4L}{(H-L)^2}}\right)\right). \tag{3.13}$$

- For $H > 0$ and $L = H$, i.e., $\Phi_E = \Phi_I$,

$$E_2 = \left(\frac{1}{1+H}, \frac{1}{1+H}\right). \tag{3.14}$$

- For $H > 0$ and $L > H$, i.e., $\Phi_E/\Phi_I > 1$,

$$E_3 = \left(\frac{1}{2}\left(\frac{H+1}{H-L} + \sqrt{\frac{(H-1)^2+4L}{(H-L)^2}}\right), \frac{1}{2}\left(2 + \frac{H(H+1)}{L-H} - H\sqrt{\frac{(H-1)^2+4L}{(H-L)^2}}\right)\right). \tag{3.15}$$

To analyze the linear stability of the equilibria, we consider the Jacobian matrix of the system (3.11):

$$J = \begin{pmatrix} -2LN^*_{\text{int}} - N^*_{\text{pyr}} & 1 - N^*_{\text{int}} \\ -HN^*_{\text{pyr}} & 1 - HN^*_{\text{int}} - 2N^*_{\text{pyr}} \end{pmatrix}, \tag{3.16}$$

which has the following eigenvalues:

$$\lambda_{1,2} = \frac{1}{2}\left(1 - (H+2L)N^*_{\text{int}} - 3N^*_{\text{pyr}} \pm \sqrt{(-1 + (H-2L)N^*_{\text{int}} + N^*_{\text{pyr}})^2 + 4H(N^*_{\text{int}} - 1)N^*_{\text{pyr}}}\right).$$

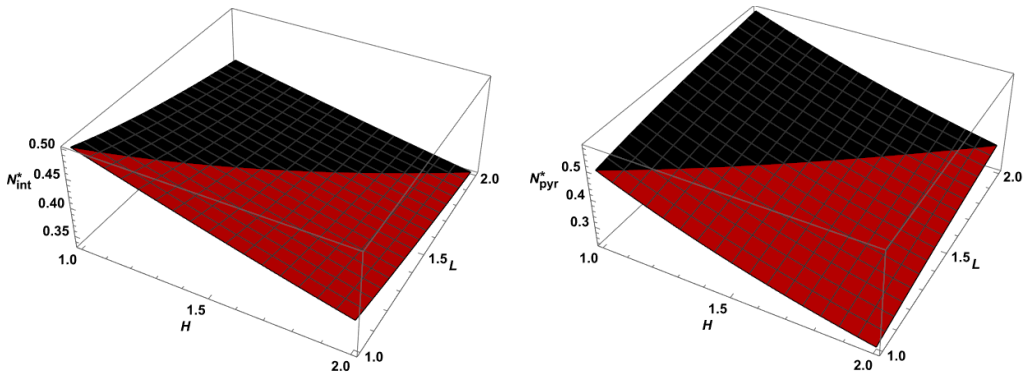

Figure 4. Plot of the equilibria as functions of H and L. The components of equilibrium $E_1 = (N^*_{\text{int},1}, N^*_{\text{pyr},1})$ are shown in red, those of E_3 in black, while the components of E_2 are located at the boundary between the surfaces representing E_1 and E_3.

Therefore, we have the following results:

- The equilibrium E_0 is always locally unstable. In fact, the Jacobian matrix evaluated at E_0 has the eigenvalues $\lambda_1 = 1, \lambda_2 = 0$.
- The equilibria E_1, E_2, E_3, if they exist, are locally asymptotically stable without any additional conditions. In particular, we have:

– The eigenvalues of the Jacobian matrix evaluated at E_1 are complex conjugates with a negative real part. Therefore, the system exhibits damped oscillatory dynamics around this steady-state.
– The Jacobian matrix evaluated at E_2 has the eigenvalues $\lambda_{1,2} = -1$.
– The eigenvalues of the Jacobian matrix evaluated at E_3 are real, distinct, and negative.

These mathematical results highlight that all count-dominated regimes, as well as the non-trivial balanced count regimes, can be realized, whereas the balanced count regime in which no interneurons or pyramidal neurons are active can never be observed.

Furthermore, in view of Eqs (3.13)–(3.15), the components of the coexistence equilibria, when they exist, exhibit specific monotonic properties, as shown in Figure 4:

- The equilibrium E_1, which corresponds to an inhibitory-count-dominated network regime, decreases with H for both components, while it increases with L for the second component and decreases for the first.
- The equilibrium E_2, which corresponds to a balanced count network regime, decreases with H.
- The equilibrium E_3, which corresponds to an excitatory-count-dominated network regime, decreases with H for both components; the second component increases with L, while the first decreases with L.

Finally, at the equilibrium E_3, the number of interneurons, i.e., the first component, is always smaller then the number of pyramidal neurons, i.e., the second component, as expected in an excitatory-count-dominated network regime. Conversely, at the equilibrium E_1, the number of interneurons is always larger than the number of pyramidal neurons, reflecting an inhibitory-count-dominated regime. The ratio Φ_E/Φ_I serves as a macroscopic indicator of whether the network operates in a count-dominated or count-balanced regime. This balance is particularly significant, as small variations in the connectivity structure and/or in the interaction probabilities affecting Φ_E/Φ_I can shift the system between regimes, leading to qualitatively different collective network dynamics.

In the remaining part of this section, we report numerical simulations that highlight the influence of connectivity and population heterogeneity on the global network dynamics and their role in inducing transitions between count-dominated regimes.

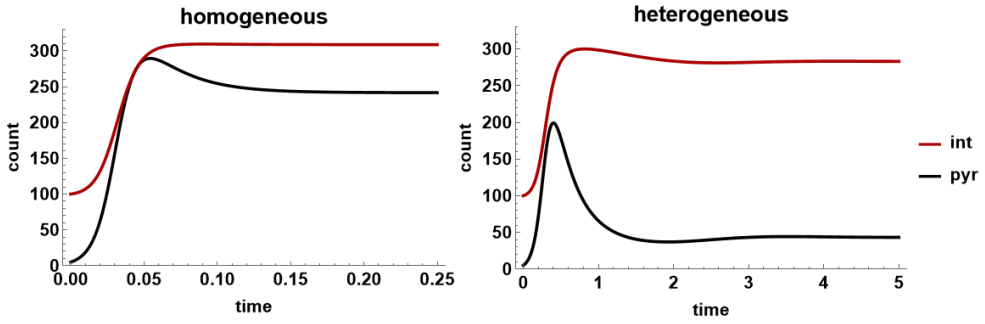

Figure 5. Network activity dynamics. The one-slice model (3.8) is numerically integrated by setting $n_{\text{int}} = 320, n_{\text{pyr}} = 1600, p_1 = 0.7, p_2 = 0.045, q_1 = 0.1, q_2 = 0.99$, and assuming a homogeneous connectivity structure with $\alpha = \beta = \delta = \gamma = 1$ (left), and a heterogeneous connectivity structure with $\alpha = 0.07, \beta = 0.12, \delta = 0.15, \gamma = 0.1$ (right). In both cases we set the initial conditions as $N^0_{\text{int}}(1) = 100$ and $N^0_{\text{pyr}}(1) = 5$.

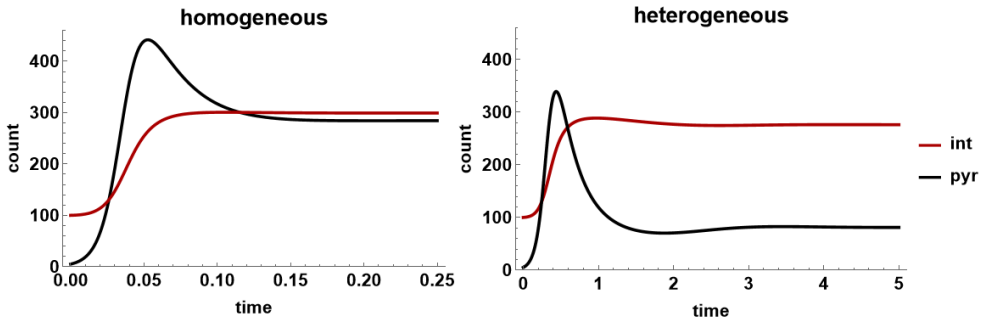

Figure 6. Network activity dynamics. System (3.8) is numerically integrated using the same parameter values as in Figure 5, except for p_1 which is set to 0.3.

Figure 5 illustrates the network activity dynamics in terms of the number of active interneurons and pyramidal neurons, for a homogeneous (Figure 5, left) and a heterogeneous (Figure 5, right) connectivity structure. Consistent with the model, for fixed transition probabilities and a given total number of interneurons and pyramidal neurons in the network, the connectivity structure influences both the network dynamics and the equilibrium values of active interneurons and pyramidal neurons. Furthermore, in the homogeneous case, the equilibrium values of active interneurons and pyramidal neurons are reached in a shorter time.

To highlight the role of transition probabilities in network dynamics, we perform a new simulation of the model, as shown in Figure 6. Specifically, we set all parameter values as in Figure 5, except for the transition probability p_1, which governs the activation of interneurons due to interactions with pyramidal neurons. By setting $p_1 = 0.3$ instead of $p_1 = 0.7$, we observe, in both the homogeneous case (Figure 6, left) and the heterogeneous case (Figure 6, right), a lower number of active interneurons and a higher number of active pyramidal neurons, consistent with the lower activation probability of the interneuron compared to the previous case.

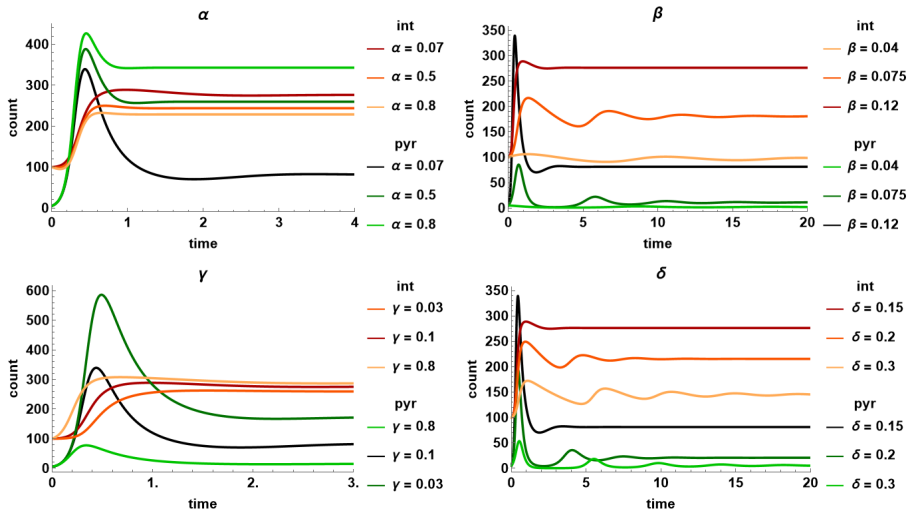

Figure 7. Effects of the connectivity structure. Different dynamics can be observed by varying the network connectivity structure in terms of the parameters $\alpha, \beta, \gamma, \delta$, which represent the fractions of int-to-int, pyr-to-pyr, pyr-to-int, and int-to-pyr connections, respectively. All other numerical parameter values are set as in Figure 6.

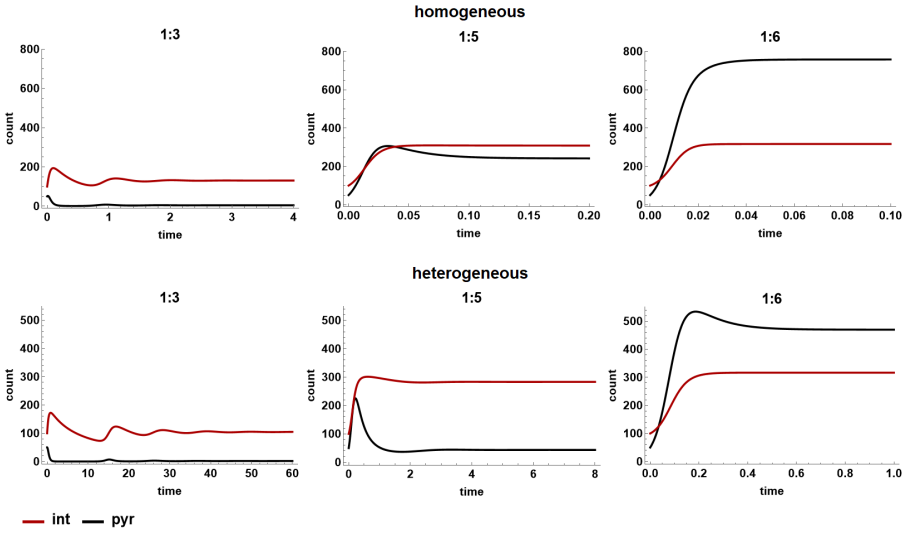

Figure 8. Effects of the balance between excitatory and inhibitory neurons. The figure illustrates how, starting from $n_{\text{int}} = 320$, varying the ratio $n_{\text{pyr}}/n_{\text{int}}$ to values of 3 (left), 5 (middle), and 6 (right) affects the network dynamics in both homogeneous (top) and heterogeneous (bottom) connectivity. All other numerical parameter values are set as in Figure 6.

In Figure 7, we illustrate the role of the parameters α, β, γ, δ, which represent the fraction of int-to-int, pyr-to-pyr, pyr-to-int, and int-to-pyr connections, respectively, in the dynamics of active interneurons and pyramidal neurons. An increase in the values of the parameters α (int-to-int connections) or β (pyr-to-pyr connections) results in enhanced excitatory activity in the network, at the expense of inhibitory activity. In contrast, the opposite effect is observed for the parameters δ and γ.

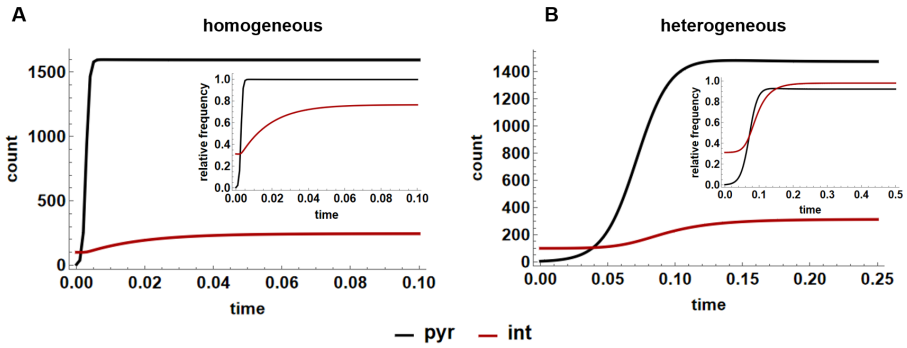

Figure 9. Dominated regime shift. Transition from an excitatory- ($\Phi_E/\Phi_I = 10^2$) to an inhibitory-count-dominated regime ($\Phi_E/\Phi_I = 0.25$), induced by heterogeneous connectivity, is illustrated. The one-slice model is numerically integrated assuming an all-to-all connectivity structure (left), and a heterogeneous connectivity (right) with $\alpha = 0.04$, $\beta = 0.04$, $\delta = \gamma = 0.8$. Other parameters are $n_{\text{int}} = 320$, $n_{\text{pyr}} = 1600$, $p_1 = 0.05$, $p_2 = 0.5$, $q_1 = 0.5$, $q_2 = 0.05$, and the initial conditions are $N^0_{\text{int}}(1) = 100$ and $N^0_{\text{pyr}}(1) = 5$.

Finally, Figure 8 explores how the balance between excitation and inhibition affects the network

dynamics. In particular, under the assumption that interneurons exert a significantly stronger modulatory effect compared to pyramidal neurons, we consider a network composed of $N = n_{\text{int}} + n_{\text{pyr}}$ neurons, with $n_{\text{pyr}}/n_{\text{int}} = 3, 5, 6$. Significantly, we observe that for $n_{\text{pyr}}/n_{\text{int}} = 3$ or 5, the equilibrium value of pyramidal neurons is lower than that of interneurons. However, when $n_{\text{pyr}}/n_{\text{int}} = 6$, the opposite occurs, with pyramidal neurons exhibiting a higher equilibrium value than interneurons, in both homogeneous (Figure 8, top) and heterogeneous (Figure 8, bottom) connectivity structures. In Figure 9, we report a case of the transition from an excitatory- ($\Phi_E/\Phi_I > 1$) to an inhibitory-count-dominated ($\Phi_E/\Phi_I < 1$) regime produced by modifying only the connectivity structure of the network. These simulations illustrate the activity of the entire network, composed of two populations of interneurons and pyramidal neurons, each characterized by fixed firing and excitability properties (i.e., p_1, p_2, q_1, q_2), and a connectivity structure defined as a percentage by the parameters α, β, γ, δ. Moreover, within this framework, the heterogeneity in both excitability and connectivity structure remains relatively limited. In the following section, we demonstrate how a constrained version of the two-slice model can reproduce the same overall network dynamics while also providing insights into the local dynamics within each slice. Finally, we will present more general dynamics of the sliced network that cannot be inferred from the one-slice model.

3.2. Two-slice model

In this section, we analyze the outcomes of the kinetic model (3.4), assuming the network consists of two interacting slices, i.e., $S = 2$. In this case, system (3.4), in view of Eq (2.25), reduces to

$$
\begin{aligned}
\frac{d}{dt}N_{1,\text{int}}(1) &= -\alpha^{w_1} q_1^{w_1} n_{1,\text{int}}^2 N_{1,\text{int}}^2(1) - \alpha^{b_{21}} q_1^{b_{21}} n_{1,\text{int}} n_{2,\text{int}} N_{1,\text{int}}(1) N_{2,\text{int}}(1) \\
&\quad + \gamma^{w_1} p_1^{w_1} n_{1,\text{pyr}} n_{1,\text{int}}^2 N_{1,\text{pyr}}(1) - \gamma^{w_1} p_1^{w_1} n_{1,\text{pyr}} n_{1,\text{int}} N_{1,\text{pyr}}(1) N_{1,\text{int}}(1) \\
&\quad + \gamma^{b21} p_1^{b_{21}} n_{2,\text{pyr}} n_{1,\text{int}}^2 N_{2,\text{pyr}}(1) - \gamma^{b21} p_1^{b_{21}} n_{2,\text{pyr}} n_{1,\text{int}} N_{2,\text{pyr}}(1) N_{1,\text{int}}(1), \\
\frac{d}{dt}N_{1,\text{pyr}}(1) &= -\delta^{w_1} q_2^{w_1} n_{1,\text{int}} n_{1,\text{pyr}} N_{1,\text{pyr}}(1) N_{1,\text{int}}(1) - \delta^{b_{21}} q_2^{b_{21}} n_{1,\text{pyr}} n_{2,\text{int}} N_{1,\text{pyr}}(1) N_{2,\text{int}}(1) \\
&\quad + \beta^{w_1} p_2^{w_1} n_{1,\text{pyr}}^3 N_{1,\text{pyr}}(1) - \beta^{w_1} p_2^{w_1} n_{1,\text{pyr}}^2 N_{1,\text{pyr}}^2(1) \\
&\quad + \beta^{b_{21}} p_2^{b_{21}} n_{2,\text{pyr}} n_{1,\text{pyr}}^2 N_{2,\text{pyr}}(1) - \beta^{b_{21}} p_2^{b_{21}} n_{2,\text{pyr}} n_{1,\text{pyr}} N_{1,\text{pyr}}(1) N_{2,\text{pyr}}(1), \\
\frac{d}{dt}N_{2,\text{int}}(1) &= -\alpha^{b_{12}} q_1^{b_{12}} n_{1,\text{int}} n_{2,\text{int}} N_{2,\text{int}}(1) N_{1,\text{int}}(1) - \alpha^{w_2} q_1^{w_2} n_{2,\text{int}}^2 N_{2,\text{int}}^2(1) \\
&\quad + \gamma^{b_{12}} p_1^{b_{12}} n_{1,\text{pyr}} n_{2,\text{int}}^2 N_{1,\text{pyr}}(1) - \gamma^{b_{12}} p_1^{b_{12}} n_{1,\text{pyr}} n_{2,\text{int}} N_{1,\text{pyr}}(1) N_{2,\text{int}}(1) \\
&\quad + \gamma^{w_2} p_1^{w_2} n_{2,\text{pyr}} n_{2,\text{int}}^2 N_{2,\text{pyr}}(1) - \gamma^{w_2} p_1^{w_2} n_{2,\text{pyr}} n_{2,\text{int}} N_{2,\text{pyr}}(1) N_{2,\text{int}}(1), \\
\frac{d}{dt}N_{2,\text{pyr}}(1) &= -\delta^{b_{12}} q_2^{b_{12}} n_{1,\text{int}} n_{2,\text{pyr}} N_{2,\text{pyr}}(1) N_{1,\text{int}}(1) - \delta^{w_2} q_2^{w_2} n_{2,\text{int}} n_{2,\text{pyr}} N_{2,\text{pyr}}(1) N_{2,\text{int}}(1) \\
&\quad + \beta^{b_{12}} p_2^{b_{12}} n_{1,\text{pyr}} n_{2,\text{pyr}}^2 N_{1,\text{pyr}}(1) - \beta^{b_{12}} p_2^{b_{12}} n_{1,\text{pyr}} n_{2,\text{pyr}} N_{1,\text{pyr}}(1) N_{2,\text{pyr}}(1) \\
&\quad + \beta^{w_2} p_2^{w_2} n_{2,\text{pyr}}^3 N_{2,\text{pyr}}(1) - \beta^{w_2} p_2^{w_2} n_{2,\text{pyr}}^2 N_{2,\text{pyr}}^2(1).
\end{aligned}
\tag{3.17}
$$

A straightforward calculation allows us to establish a complete equivalence between system (3.8) and a constrained version of system (3.17). Specifically, by assuming $n_{i,\text{int}} = n_{\text{int}}/A_i$, $n_{i,\text{pyr}} = n_{\text{pyr}}/B_i$, for

$i = 1, 2$, and imposing the following conditions for all $i, j = 1, 2$:

$$p_1^{w_i} = p_1^{b_{ij}} = p_1^{b_{ji}} = p_1, \quad p_2^{w_i} = p_2^{b_{ij}} = p_2^{b_{ji}} = p_2, \quad q_1^{w_i} = q_1^{b_{ij}} = q_1^{b_{ji}} = q_1, \quad q_2^{w_i} = q_2^{b_{ij}} = q_2^{b_{ji}} = q_2. \tag{3.18}$$

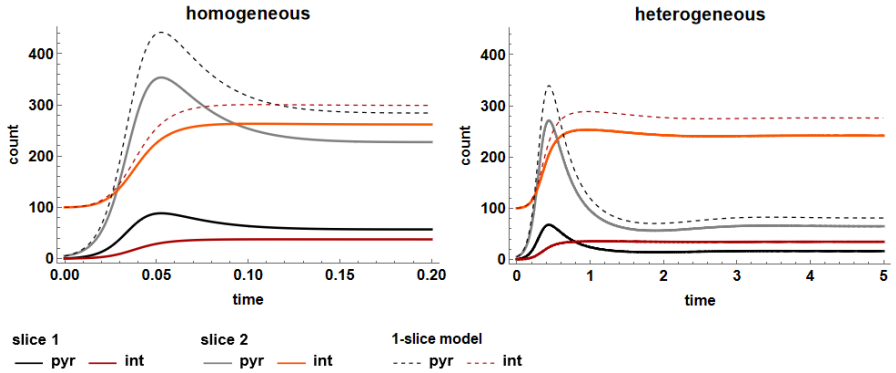

Figure 10. Constrained two-slice network activity dynamics. The two-slice model (3.17) is numerically integrated under the constraints (3.18) and (3.19), and the overall network dynamics are compared with the dynamics of each slice. We set $A_1 = 8, A_2 = 8/7, B_1 = 5$, and $B_2 = 5/4$, while all the remaining parameters are fixed as in Figure 6. In both cases we set the initial conditions as $N^0_{1,\text{int}}(1) = 100, N^0_{1,\text{pyr}}(1) = 5$, and $N^0_{2,\text{int}}(1) = N^0_{2,\text{pyr}}(1) = 0$.

Equation (3.17) reduces to Eq (3.8) provided that, for all $i, j = 1, 2$, the following constraints hold:

$$\begin{aligned} &\alpha^{w_i} = A_i^2\alpha, \quad \alpha^{b_{ij}} = A_iA_j\alpha, \quad &&\beta^{w_i} = B_i^2\beta, \quad \beta^{b_{ij}} = B_iB_j\beta, \\ &\delta^{w_i} = A_iB_i\delta, \quad \delta^{b_{ij}} = A_iB_j\delta, \quad &&\gamma^{w_i} = A_iB_i\gamma, \quad \gamma^{b_{ij}} = A_jB_i\gamma. \end{aligned} \tag{3.19}$$

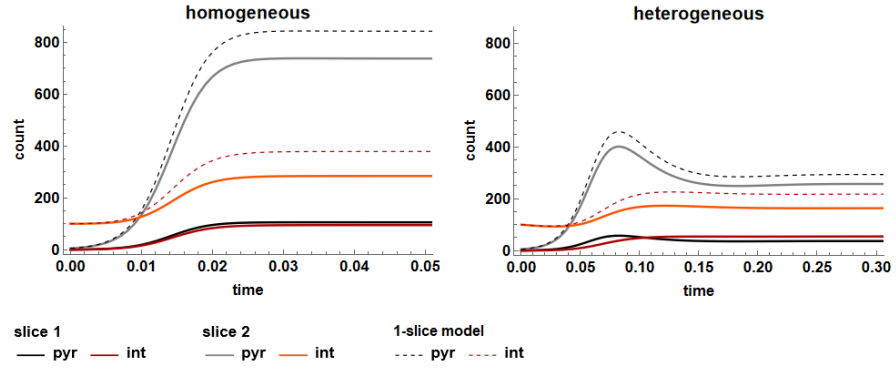

Figure 11. Constrained two-slice network activity dynamics. The two-slice model (3.17) is numerically integrated under the constraints (3.18) and (3.19), by setting $n_{\text{int}} = 400, 320, n_{\text{pyr}} = 1600, A_1 = 4, A_2 = 4/3, B_1 = 8, B_2 = 8/7, p_1 = 0.6, p_2 = 0.1, q_1 = 0.3, q_2 = 0.8$, and assuming a homogeneous connectivity structure with $\alpha = \beta = \delta = \gamma = 1$ (left), and a heterogeneous connectivity structure with $\alpha = 0.9, \beta = 0.3, \delta = 0.9, \gamma = 0.1$ (right). In both cases we set the initial conditions as $N^0_{1,\text{int}}(1) = N^0_{1,\text{pyr}}(1) = 0$, and $N^0_{2,\text{int}}(1) = 100$, and $N^0_{2,\text{pyr}}(1) = 5$.

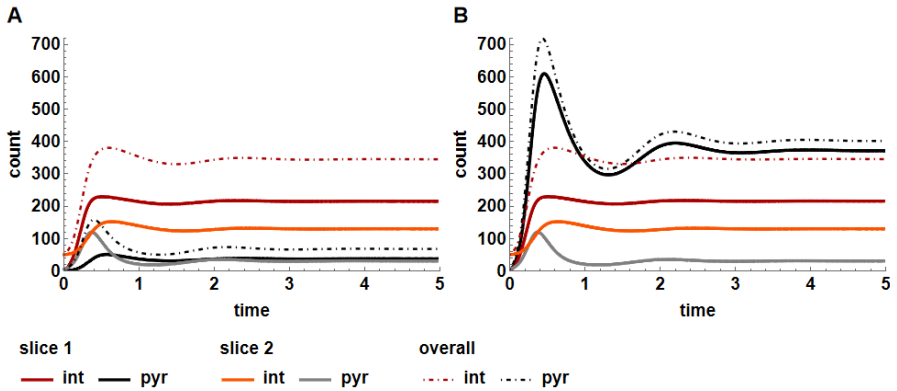

Figure 12. Two-slice network activity dynamics. System (3.17) is numerically integrated by setting $n_{1,\text{int}} = n_{2,\text{int}} = 240$, $n_{1,\text{pyr}} = n_{2,\text{pyr}} = 1200$, $p_1^{w_1} = 0.01$, $p_2^{w_1} = 0.045$, $q_1^{w_1} = 0.1$, $q_2^{w_1} = 0.01$, $p_1^{w_2} = 0.9$, $p_2^{w_2} = 0.1$, $q_1^{w_2} = 0.1$, $q_2^{w_2} = 0.9$, $p_1^{b_{12}} = 0.1$, $p_1^{b_{21}} = 0.9$, $q_1^{b_{12}} = 0.1$, $q_2^{b_{12}} = 0.99$, $p_2^{b_{21}} = 0.1$, $p_2^{b_{12}} = 0.045$, $q_1^{b_{21}} = 0.1$, and $q_2^{b_{21}} = 0.9$, the within-slice connectivity structure $\alpha^{w_1} = 0.07$, $\beta^{w_1} = 0.05$, $\gamma^{w_1} = 0.1$, $\delta^{w_1} = 0.15$, $\alpha^{w_2} = 0.9$, $\beta^{w_2} = 0.12$, $\gamma^{w_2} = 0.1$, $\delta^{w_2} = 0.6$, and the between-slice connectivity $\alpha^{b_{21}} = 0.5$, $\gamma^{b_{21}} = 0.5$, $\delta^{b_{21}} = 0.15$. Additionally, we set $\beta^{b_{21}} = 0.01$ for the left panel and $\beta^{b_{21}} = 0.25$ for the right panel. In both cases we set the initial conditions as $N^0_{1,\text{int}}(1) = N^0_{1,\text{pyr}}(1) = 0$, and $N^0_{2,\text{int}}(1) = 50$, and $N^0_{2,\text{pyr}}(1) = 5$.

In Figure 10, we examine the overall network dynamics when the network is composed of two different slices. We assume that slice 1 consists of only 1/8 of the total interneurons and 1/5 of the total pyramidal neurons. System (3.17) is numerically integrated under the constraints (3.18) and (3.19), with the numerical values of parameters as set in Figure 6. Initially, only interneurons and pyramidal neurons belonging to slice 1 are activated. Although the transition probabilities remain homogeneous for each type of interaction (pyr-to-pyr, int-to-pyr, pyr-to-int, and int-to-int) in both slices, it is possible to observe how the connectivity structure affects both the dynamics within each slice and the overall network dynamics. Moreover, when a homogeneous connectivity structure is assumed, the overall dynamics differ slightly from those of each individual slice (Figure 10, left). In particular, the long-term values of the total number of active pyramidal neurons are slightly lower compared to the interneurons (black and red dashed lines in Figure 10, left), but this property is observed only in slice 2 (gray and orange lines in Figure 10, left), and not in slice 1 (black and red lines in Figure 10, left), where the behavior is opposite.

Another comparison between the one-slice and constrained two-slice models is presented in Figure 11. In particular, we highlight the influence of the connectivity structure on network dynamics, both globally and locally within each slice. Under homogeneous connectivity, both interneurons and pyramidal neurons exhibit a classical S-shaped growth pattern (Figure 11, left). In contrast, with heterogeneous connectivity, the dynamics are no longer monotonically increasing, leading to more complex interactions between the two neuronal populations, both at the global network level (black and red dashed lines in Figure 11, right) and within each slice (colored continuous lines in Figure 11, right). The section concludes with a two-slice model simulation where the overall network dynamics cannot be inferred from the one-slice model, as conditions (3.18) and (3.19) are not satisfied (see Figure 12). We consider a network composed of two slices that are identical only in terms of the number of interneurons and pyramidal neurons, i.e., $n_{1,\text{int}} = n_{2,\text{int}} = 1200$ and $n_{1,\text{pyr}} = n_{2,\text{pyr}} = 240$,

but are characterized by neuronal populations that inherently differ in both their firing and excitability properties, as well as in their connectivity structure. We focus on a heterogeneous and asymmetrical network connectivity structure, where slice 2 is (heterogeneously) connected to slice 1, but not vice versa, i.e., $\alpha^{b_{12}} = \beta^{b_{12}} = \gamma^{b_{12}} = \delta^{b_{12}} = 0$ (Figure 12, left). First, we examine the case where the pyramidal neurons of slice 2 are weakly connected to the pyramidal neurons of slice 1, i.e., $\beta^{b_{21}} = 0.01$ (Figure 12, right), and then we increase this type of connectivity by setting $\beta^{b_{21}} = 0.25$. As expected, the increase in the parameter $\beta^{b_{21}}$ affects only the dynamics of slice 1 (Figure 12, red and black continuous lines) and, consequently, the overall network dynamics (Figure 12, black and red dot-dashed lines). In particular, this modification of the connectivity structure results in a higher number of active pyramidal neurons compared to both the previous case and the number of active interneurons in both scenarios. This highlights how a modification in the connectivity structure can unbalance the overall excitation or inhibition of the network.

3.3. Four-slice model

In this section, we consider the four-slice model, which can be derived from Eq (3.4) by setting $S = 4$. As the number of slices increases, predicting a priori the dynamics of active interneurons and pyramidal neurons becomes increasingly challenging due to the complex cumulative effects of the model parameters on both local and global network dynamics.

To address this, we perform numerical simulations exclusively on the four-slice model to highlight the fundamental role of connectivity structure in shaping network dynamics. Specifically, we fix firing, excitability, and inhibition properties of the four neuronal populations and analyze both local and global network behaviors solely as a function of the connectivity structure, distinguishing between homogeneous and heterogeneous cases. Given the high dimensionality of the input parameters in these simulations, we summarize them in tables (see Table 2), which serve as the fundamental reference for the input data to be associated with the Python code* provided with the paper (see Supplementary). For both simulations, we first consider a network with homogeneous connectivity, resulting in strongly excitatory network dynamics (Figure 13, left panels). Then, we demonstrate how introducing a heterogeneous and asymmetrical connectivity structure may not only modify local and global network dynamics (see Figure 13, right panels) but, in a specific case, even transform the excitatory-count-dominated nature of the network into a predominantly inhibitory-count one (Figure 13, lower right panel).

Specifically, to highlight the impact of connectivity structure on network dynamics, we first consider a homogeneous connectivity setup for four identical excitatory and inhibitory neuronal populations in terms of neuron count, introducing only slight heterogeneity in transition probabilities $p_1^{w_h}$, $p_2^{w_h}$, $q_1^{w_h}$, $q_2^{w_h}$ (within-slice) and $p_1^{b_{hk}}$, $p_2^{b_{hk}}$, $q_1^{b_{hk}}$, $q_2^{b_{hk}}$ (between-slice). For this purpose, we set all model parameters as in Table 2, except for the connectivity parameters—α^{w_h}, β^{w_h}, γ^{w_h}, δ^{w_h} (within-slice) and $\alpha^{b_{hk}}$, $\beta^{b_{hk}}$, $\gamma^{b_{hk}}$, $\delta^{b_{hk}}$ (between-slice)—which are all fixed at 1 (i.e., 100% in percentage terms) for panel A of Figure 13, and with $\alpha^{w_h} = \alpha^{b_{hk}} = 1$, $\beta^{w_h} = \beta^{b_{hk}} = 1, \gamma^{w_h} = \gamma^{b_{hk}} = 0.1$, $\delta^{w_h} = \delta^{b_{hk}} = 0.2$ for panel B of Figure 13. As expected, interneurons and pyramidal neurons within each slice exhibit similar dynamic trends (Figure 13, middle panels). In particular, the activity of pyramidal neurons in each slice undergoes a slight decline after an initial peak, coinciding with an increase in the number of active interneurons within the slices (Figure 13, middle panels). However, in case A with all-to-all connectivity, the network is inhibitory-count-dominated ($\Phi_E/\Phi_I = 0.63$), whereas in case B with homogeneous connectivity, it

*Python code is available at the ModelDB section of the Senselab database (https://modeldb.science/2020339).

operates in an excitatory-count-dominated regime ($\Phi_E/\Phi_I = 1.28$) (Figure 13 left panels, continuous curves), but only in case A the network activity remains excitatory-count-dominated ($\Phi_E/\Phi_I = 0.18$). Introducing a heterogeneous and asymmetric connectivity structure significantly alters the dynamics of the network (Figure 13, middle panels). Notably, in case B (middle pane) the initial peak in pyramidal neuron activity is followed by a sharp decline accompanied by damped oscillations, in contrast to the sustained excitatory response observed in the homogeneous condition (Figure 13, bottom right panel).

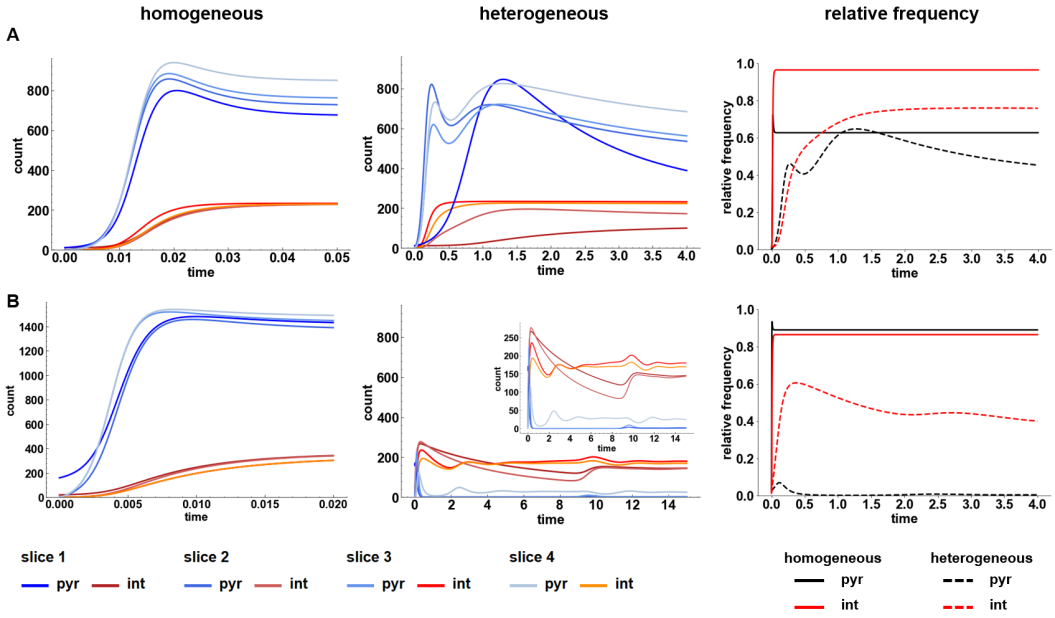

Figure 13. Four-slice network activity dynamics. Dynamics of active interneurons and pyramidal neurons in a four-slice networks with homogeneous (left) and heterogeneous (middle) connectivity structures. Panel A: Homogeneous connectivity results in a rapid increase in neuronal activity for both interneurons and pyramidal neurons, followed by a plateau, reflecting an inhibitory-count-dominated regime. Although heterogeneous connectivity (middle panel) induces an initial peak in pyramidal neurons activity followed by a sharp decline highlighting the impact of connectivity structure on network dynamics, the inhibitory-count-dominated regime persists (left). Panel B: Under homogeneous connectivity (left), all four slices exhibit similar activity patterns, with a stabilization after an initial rise. In the heterogeneous network (middle), the introduction of asymmetric connection strengths leads to substantial variability across slices, with pronounced oscillatory behavior and a shift toward a predominantly inhibitory-count-dominated network state (lower middle panel). The inset further emphasizes the sustained suppression of the pyramidal neurons activity, and how an increased heterogeneity on the connectivity structure may drive the network toward an inhibitory-count-dominated regime. The input parameters used for these numerical simulations are reported in Table 2, with the exception of parameters related to the homogeneous connectivity structure ($\alpha^{w_h}, \beta^{w_h}, \gamma^{w_h}, \delta^{w_h}$ (within-slice) and $\alpha^{b_{hk}}, \beta^{b_{hk}}, \gamma^{b_{hk}}, \delta^{b_{hk}}$ (between-slice)), which need to be set to 100% for the dynamics reported in the top right panel and with $\alpha^{w_h} = \alpha^{b_{hk}} = \beta^{w_h} = \beta^{b_{hk}} = 100\%$, $\gamma^{w_h} = \gamma^{b_{hk}} = 10\%$, $\delta^{w_h} = \delta^{b_{hk}} = 20\%$ for panel B.

Table 2. Input parameters for the four-slice network model of Figure 13. The table summarizes the input parameters used for the numerical simulations of the four-slice network model shown in Figure 13 (right panels), including neuron counts (panels A and B, top left), initial conditions (panels A and B, top right), connectivity structures (panels A and B, middle), and transition probabilities (panels A and B, bottom) for the neuronal populations within and between the four slices. For the simulations involving homogeneous network connectivity (Figure 13, left panels), all parameters related to the connectivity structure of panel A (panels A and B, middle) need to be set to 100% and to $\alpha^{w_h} = \alpha^{b_{hk}} = \beta^{w_h} = \beta^{b_{hk}} = 100\%$, $\gamma^{w_h} = \gamma^{b_{hk}} = 10\%$, $\delta^{w_h} = \delta^{b_{hk}} = 20\%$ for panel B. Due to the asymmetrical properties of the network, the red arrows indicate the direction of the interactions, which are organized row-wise from left to right.

A

	neuron counts		initial conditions % active	
	n_{int}	n_{pyr}	% int	% pyr
slice 1	240	1200	5%	1%
slice 2	240	1200	0%	0%
slice 3	240	1200	0%	0%
slice 4	240	1200	0%	0%

connectivity structure

α (int-to-int)

→	slice 1	slice 2	slice 3	slice 4
slice 1	30%	70%	2%	0%
slice 2	0%	30%	5%	2%
slice 3	0%	0%	20%	5%
slice 4	0%	0%	0%	20%

β (pyr-to-pyr)

→	slice 1	slice 2	slice 3	slice 4
slice 1	5%	30%	30%	30%
slice 2	0%	12%	10%	10%
slice 3	0%	5%	5%	0%
slice 4	0%	0%	0%	5%

γ (pyr-to-int)

→	slice 1	slice 2	slice 3	slice 4
slice 1	10%	5%	5%	0%
slice 2	0%	10%	10%	5%
slice 3	0%	5%	5%	5%
slice 4	0%	0%	5%	5%

δ (int-to-pyr)

→	slice 1	slice 2	slice 3	slice 4
slice 1	15%	15%	5%	0%
slice 2	0%	60%	10%	5%
slice 3	0%	5%	20%	5%
slice 4	0%	5%	5%	20%

transition probabilities

p_1 (pyr-to-int)

→	slice 1	slice 2	slice 3	slice 4
slice 1	0.01	0.1	0.1	0.3
slice 2	0.1	0.02	0.1	0.3
slice 3	0.3	0.3	0.03	0.3
slice 4	0.1	0.1	0.1	0.3

q_1 (int-to-int)

→	slice 1	slice 2	slice 3	slice 4
slice 1	0.05	0.1	0.1	0.1
slice 2	0.1	0.1	0.1	0.1
slice 3	0.1	0.1	0.1	0.1
slice 4	0.1	0.1	0.1	0.1

p_2 (pyr-to-pyr)

→	slice 1	slice 2	slice 3	slice 4
slice 1	0.07	0.045	0.045	0.045
slice 2	0.1	0.1	0.045	0.045
slice 3	0.045	0.045	0.1	0.1
slice 4	0.045	0.045	0.1	0.1

q_2 (int-to-pyr)

→	slice 1	slice 2	slice 3	slice 4
slice 1	0.99	0.99	0.3	0.3
slice 2	0.9	0.9	0.9	0.3
slice 3	0.3	0.9	0.7	0.9
slice 4	0.3	0.3	0.7	0.7

B

	neuron counts		initial conditions % active	
	n_{int}	n_{pyr}	% int	% pyr
slice 1	400	1600	5%	10%
slice 2	400	1600	0%	0%
slice 3	400	1600	0%	0%
slice 4	400	1600	0%	0%

connectivity structure

α (int-to-int)

→	slice 1	slice 2	slice 3	slice 4
slice 1	7%	5%	2%	0%
slice 2	0%	7%	5%	2%
slice 3	0%	0%	7%	5%
slice 4	0%	0%	0%	7%

β (pyr-to-pyr)

→	slice 1	slice 2	slice 3	slice 4
slice 1	5%	0%	5%	0%
slice 2	5%	5%	10%	5%
slice 3	0%	5%	5%	0%
slice 4	0%	0%	0%	5%

γ (pyr-to-int)

→	slice 1	slice 2	slice 3	slice 4
slice 1	10%	10%	5%	0%
slice 2	5%	10%	10%	5%
slice 3	0%	5%	5%	5%
slice 4	0%	0%	5%	5%

δ (int-to-pyr)

→	slice 1	slice 2	slice 3	slice 4
slice 1	15%	10%	5%	0%
slice 2	15%	15%	10%	5%
slice 3	5%	15%	20%	5%
slice 4	0%	5%	5%	20%

transition probabilities

p_1 (pyr-to-int)

→	slice 1	slice 2	slice 3	slice 4
slice 1	0.7	0.3	0.3	0.3
slice 2	0.3	0.7	0.3	0.3
slice 3	0.3	0.3	0.3	0.3
slice 4	0.3	0.3	0.3	0.3

q_1 (int-to-int)

→	slice 1	slice 2	slice 3	slice 4
slice 1	0.05	0.05	0.1	0.1
slice 2	0.05	0.05	0.1	0.1
slice 3	0.1	0.1	0.1	0.1
slice 4	0.1	0.1	0.1	0.1

p_2 (pyr-to-pyr)

→	slice 1	slice 2	slice 3	slice 4
slice 1	0.045	0.045	0.045	0.045
slice 2	0.045	0.045	0.045	0.045
slice 3	0.045	0.045	0.1	0.1
slice 4	0.045	0.045	0.1	0.1

q_2 (int-to-pyr)

→	slice 1	slice 2	slice 3	slice 4
slice 1	0.99	0.3	0.3	0.3
slice 2	0.3	0.99	0.9	0.3
slice 3	0.3	0.9	0.7	0.9
slice 4	0.3	0.3	0.7	0.7

This effect is particularly evident in the lower middle panel, where the introduction of heterogeneity results in a predominantly inhibitory-count-dominated network state ($\Phi_E/\Phi_I = 0.0032$), characterized by prolonged suppression of pyramidal neuron activity and a relative increase in oscillatory interneuron activity. The inset in the lower middle panel further highlights this shift, showing a sustained inhibition of pyramidal neuron activity over time.

These findings highlight the crucial role of connectivity structure in shaping network dynamics, with increased heterogeneity potentially driving a transition from an excitatory-count-dominated to an inhibitory-count-dominated regime. In the final simulation of the four-slice network, we show that, starting from an all-to-all connectivity structure in an inhibitory-count-dominated network ($\Phi_E/\Phi_I = 0.07$), a heterogeneous configuration can either preserve the inhibitory-count-dominated

regime ($\Phi_E/\Phi_I = 0.1$, panel B of Figure 14) or shift the network to an excitatory-count-dominated regime ($\Phi_E/\Phi_I = 1.27$, panel C of Figure 14). A similar finding is observed for a network with the same heterogeneous connectivity as in panel C when the interaction probabilities are modified ($\Phi_E/\Phi_I = 0.24$, panel D of Figure 14). This illustrates how modifications in connectivity and/or transition probabilities—potentially associated with pathological conditions—can drive transitions between distinct count-dominated network regimes. All parameters used in the four-slice network simulations of Figure 14 are set according to Table 3.

Table 3. Input parameters for the four-slice network model of Figure 14. The table reports neuron counts and initial conditions (top left), transition probabilities (bottom left), and connectivity structures (right) of the network. For simulations with homogeneous connectivity (panel A of Figure 14), all connectivity-related parameters are set to 100%.

	neuron counts	
	N_{int}	N_{pyr}
slice 1	200	800
slice 2	240	1200
slice 3	280	1000
slice 4	400	600

	initial conditions % active	
	% int	% pyr
slice 1	5%	1%
slice 2	0%	0%
slice 3	0%	0%
slice 4	0%	0%

A - B - C transition probabilities

ρ_1 (pyr-to-int)

→	slice 1	slice 2	slice 3	slice 4
slice 1	0.01	0.1	0.1	0.3
slice 2	0.1	0.02	0.1	0.3
slice 3	0.3	0.3	0.03	0.3
slice 4	0.1	0.1	0.1	0.3

q_1 (int-to-int)

→	slice 1	slice 2	slice 3	slice 4
slice 1	0.05	0.1	0.1	0.1
slice 2	0.1	0.1	0.1	0.1
slice 3	0.1	0.1	0.1	0.1
slice 4	0.1	0.1	0.1	0.1

p_2 (pyr-to-pyr)

→	slice 1	slice 2	slice 3	slice 4
slice 1	0.07	0.045	0.045	0.045
slice 2	0.1	0.1	0.045	0.045
slice 3	0.045	0.045	0.1	0.1
slice 4	0.045	0.045	0.1	0.1

q_2 (int-to-pyr)

→	slice 1	slice 2	slice 3	slice 4
slice 1	0.99	0.99	0.3	0.3
slice 2	0.9	0.9	0.9	0.3
slice 3	0.3	0.9	0.7	0.9
slice 4	0.3	0.3	0.7	0.7

B connectivity structure

α (int-to-int)

→	slice 1	slice 2	slice 3	slice 4
slice 1	30%	70%	2%	0%
slice 2	0%	30%	5%	2%
slice 3	0%	0%	20%	5%
slice 4	0%	0%	0%	20%

β (pyr-to-pyr)

→	slice 1	slice 2	slice 3	slice 4
slice 1	5%	30%	30%	30%
slice 2	0%	12%	10%	10%
slice 3	0%	5%	5%	0%
slice 4	0%	0%	0%	5%

γ (pyr-to-int)

→	slice 1	slice 2	slice 3	slice 4
slice 1	10%	5%	5%	0%
slice 2	0%	10%	10%	5%
slice 3	0%	5%	5%	5%
slice 4	0%	0%	5%	5%

δ (int-to-pyr)

→	slice 1	slice 2	slice 3	slice 4
slice 1	15%	15%	5%	0%
slice 2	0%	60%	10%	5%
slice 3	0%	5%	20%	5%
slice 4	0%	5%	5%	20%

D transition probabilities

ρ_1 (pyr-to-int)

→	slice 1	slice 2	slice 3	slice 4
slice 1	0.01	0.1	0.1	0.3
slice 2	0.1	0.02	0.1	0.3
slice 3	0.3	0.3	0.03	0.3
slice 4	0.1	0.1	0.1	0.3

q_1 (int-to-int)

→	slice 1	slice 2	slice 3	slice 4
slice 1	0.05	0.1	0.1	0.1
slice 2	0.1	0.1	0.1	0.1
slice 3	0.1	0.1	0.1	0.1
slice 4	0.1	0.1	0.1	0.1

p_2 (pyr-to-pyr)

→	slice 1	slice 2	slice 3	slice 4
slice 1	0.07	0.045	0.045	0.045
slice 2	0.1	0.1	0.045	0.045
slice 3	0.045	0.045	0.1	0.1
slice 4	0.045	0.045	0.1	0.1

q_2 (int-to-pyr)

→	slice 1	slice 2	slice 3	slice 4
slice 1	0.99	0.99	0.3	0.3
slice 2	0.9	0.9	0.9	0.3
slice 3	0.3	0.9	0.7	0.9
slice 4	0.3	0.3	0.7	0.7

C - D connectivity structure

α (int-to-int)

→	slice 1	slice 2	slice 3	slice 4
slice 1	30%	70%	5%	10%
slice 2	3%	30%	10%	2%
slice 3	5%	11%	20%	10%
slice 4	0%	17%	10%	20%

β (pyr-to-pyr)

→	slice 1	slice 2	slice 3	slice 4
slice 1	15%	30%	30%	30%
slice 2	15%	12%	10%	10%
slice 3	12%	15%	15%	5%
slice 4	10%	12%	15%	15%

γ (pyr-to-int)

→	slice 1	slice 2	slice 3	slice 4
slice 1	2%	1%	1%	0%
slice 2	0%	2%	2%	1%
slice 3	0%	1%	2%	2%
slice 4	0%	0%	2%	2%

δ (int-to-pyr)

→	slice 1	slice 2	slice 3	slice 4
slice 1	15%	15%	5%	0%
slice 2	0%	40%	10%	5%
slice 3	0%	5%	20%	5%
slice 4	0%	3%	5%	20%

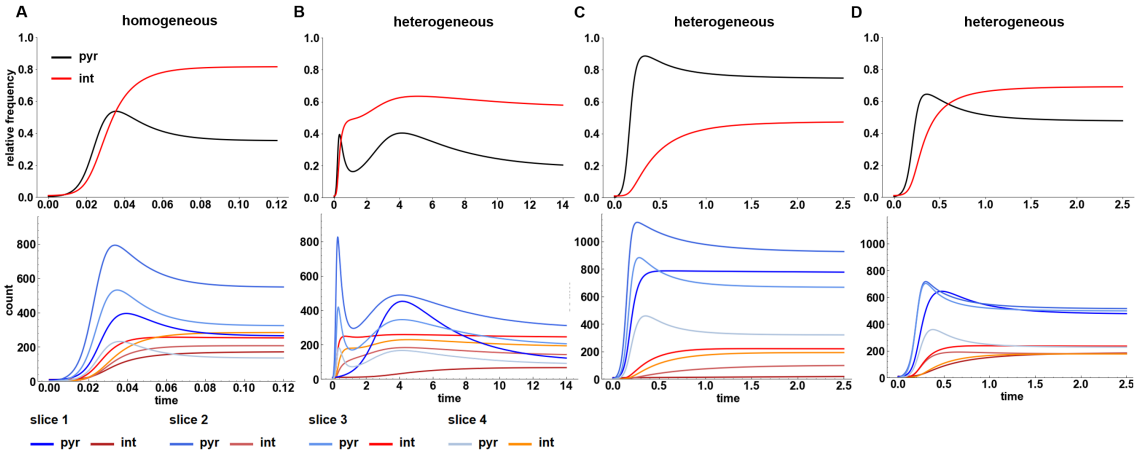

Figure 14. Count-dominated regime shift in a four-slice network. Starting from an all-to-all connectivity structure in an inhibitory-count-dominated network (panel A), a heterogeneous connectivity configuration can either preserve the inhibitory-count-dominated regime (panel B) or shift the network to an excitatory-count-dominated regime (panel C). Moreover, the network in panel D becomes inhibitory-count-dominated when the transition probabilities are altered compared to panel C, while the connectivity structure remains identical.

3.4. External inputs

In this section, we report some numerical simulations for one- and four-slice models in the presence of external inputs, representing input from other regions of the nervous system. As shown in the previous sections, for any fixed input, the one-slice model exhibits internal attractor dynamics, each characterized by its own basin of attraction. In particular, when a fixed initial number of active neurons lies within a given basin, the dynamics converge to the corresponding attractor in the absence of external inputs (Figures 5–14). However, in the presence of external inputs, the dynamics may alternate between attractors, generating oscillatory patterns of active neurons, which can also persist around asymptotically stable equilibria.

Compatible with our framework, and for simplicity considering the one-slice model, we model external input arriving at the network neurons at time $t_h - \Delta$ by imposing that, at time t_h, a fraction $\eta_E(t_h)\ N_{\rm pyr}(t_h, 0)$ and $\eta_I(t_h)\ N_{\rm int}(t_h, 0)$ of inactive interneurons and pyramidal neurons become active, respectively. To model time-varying input intensities, we set $\eta_i(t_h)$ for $i = I, E$, as either a constant value or a time-dependent function. In detail, we define $\eta_i(t_h) = f_i, i = I, E$, or according to the following law:

$$\eta_i(t_h) = f_i \left[\sin\left(a_i\, t_h^{s_i}\right)\right]^{2r_i}, \qquad i = I, E, \tag{3.20}$$

where f_i represents the maximum percentage of involved inactive neurons, and the parameters a_i, s_i, and r_i are all positive. Moreover, the sequence of times t_h at which each external input arrives can be generated either periodically (with one or multiple frequencies) or randomly.

Then, the network dynamics over the interval $[t_0, T]$, in the presence of external inputs arriving at times $t_1 - \Delta, \ldots, t_M - \Delta$, is computed by solving a sequence of M Cauchy problems on the subintervals $[t_0, t_1), [t_1, t_2), \ldots, [t_M, T]$. At each input time t_h, the initial data for active interneurons $N_{\rm int}(t_h, 1)$ and

pyramidal neurons $N_{\text{pyr}}(t_h, 1)$ are updated to account for the external stimulation as follows:

$$\begin{aligned} N_{\text{int}}(t_h, 1) &= N_{\text{int}}(t_h^-, 1) + \eta_I(t_h)\, N_{\text{int}}(t_h^-, 0), \qquad h = 1, \cdots, M, \\ N_{\text{pyr}}(t_h, 1) &= N_{\text{pyr}}(t_h^-, 1) + \eta_E(t_h)\, N_{\text{pyr}}(t_h^-, 0), \end{aligned} \tag{3.21}$$

where $t_h^- = t_h - \Delta$, $N_{\text{int}}(t_h^-, 0) = n_{\text{int}} - N_{\text{int}}(t_h^-, 1)$, and $N_{\text{pyr}}(t_h^-, 0) = n_{\text{pyr}} - N_{\text{pyr}}(t_h^-, 1)$ denote the number of inactive interneurons and pyramidal neurons, respectively.

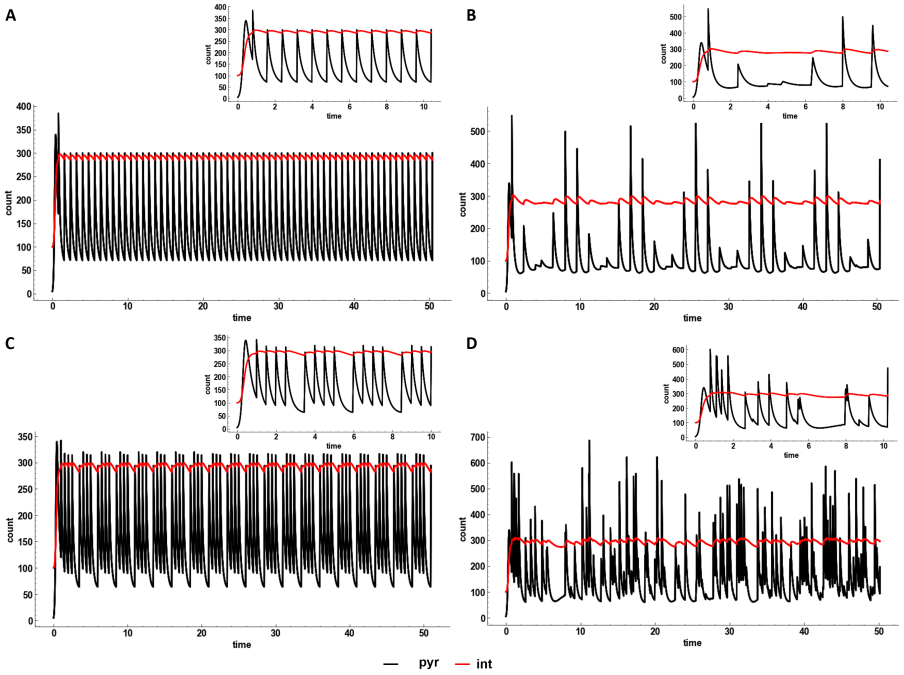

Figure 15. Oscillatory network dynamics induced by external inputs in the one-slice model. Different collective and oscillatory dynamics emerge when external inputs are applied, ranging from periodic oscillations (panels A and B) to regular and intermittent bursting activity (panels C and D). The external input parameters used in all panels are summarized in Table 4. Each inset highlights the network dynamics within a shorter time interval.

It should be evident that, within each of the above time intervals, all the qualitative and quantitative results concerning the solutions and equilibria still hold. Similarly, the same procedure can be applied when the number S of slices is greater than one. However, in this case, it is also possible to simulate scenarios in which only the neurons of one or more specific slices are affected by external inputs, for example, when such inputs originate from brain regions connected exclusively to those slices.

In the rest of this section, we report two sets of numerical simulations with external inputs for the one- and four-slice models. First, we consider the one-slice model previously analyzed in Figure 6, and additionally assume that a series of external inputs arrive at times $t_h - \Delta$, activating fractions $\eta_E(t_h)\, N_{\text{pyr}}(t_h, 0)$ and $\eta_I(t_h)\, N_{\text{int}}(t_h, 0)$ of inactive pyramidal neurons and interneurons, respectively, as summarized in Table 4, which applies to all panels of Figure 15.

The inclusion of different external inputs generates a variety of network oscillations resembling those observed in various brain areas. In particular, external stimulation governs transitions among distinct dynamical states of the network, ranging from constant and time-varying periodic oscillations (panels A

and B, respectively) to periodic constant and randomly time-varying bursting activity (panels C and D, respectively). It is evident that the emergence of these oscillatory dynamics critically depends on the duration and strength of the external inputs, as well as on the intrinsic dynamical regime of the network in absence of external stimulations. In particular, the network dynamics shown in Figure 6 (right panel) exhibit an asymptotically persistent state. Consequently, the oscillatory patterns observed in Figure 15, induced by external inputs, tend to persist around these asymptotically stable equilibria. Following any external perturbation, the system rapidly relaxes back to equilibrium, unless further inputs are delivered (see Figure S1). A systematic investigation of how specific collective dynamics arise as a function of input duration and strength, as well as functional and connectivity heterogeneity, will be addressed in a future study. We then focus on the four-slice model to show that comparable oscillatory dynamics emerge even when external inputs target only a single slice, as expected for anatomically defined network subdivisions. To this end, we consider the heterogeneous four-slice network shown in Figure 13, panel A (middle), and restrict the external inputs to slice 1, as detailed in Table 4.

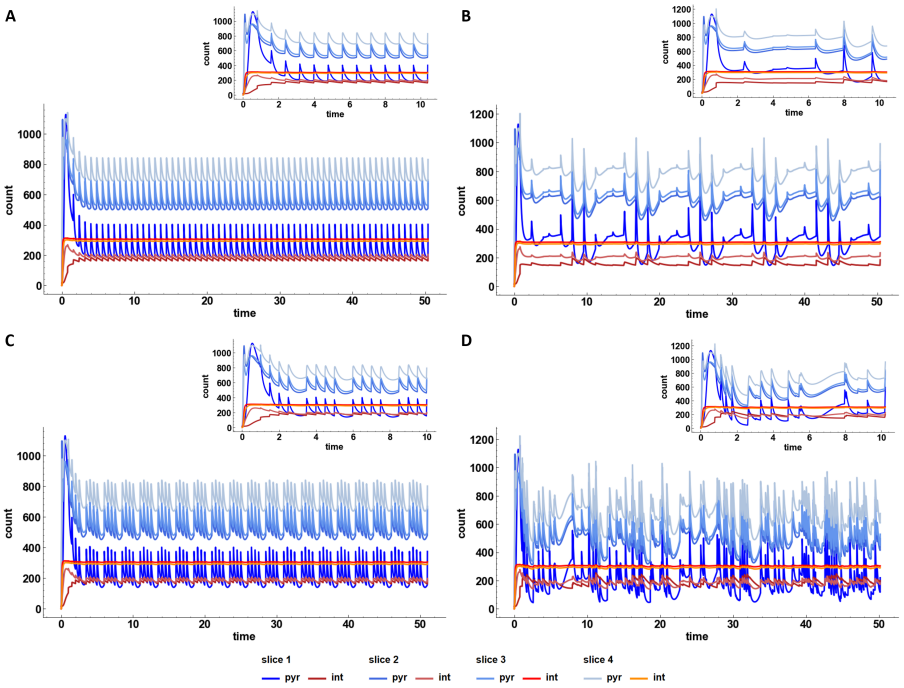

Figure 16. Oscillatory network dynamics induced by external inputs in the four-slice model. Oscillatory dynamics emerge when external inputs are applied only to slice 1. Due to the connectivity and interaction probabilities, these oscillations propagate to all other slices. Depending on the external inputs, the dynamics of all slices are characterized by periodic oscillations (panels A and B) or by regular and intermittent bursting activity (panels C and D). The external input parameters used in all panels, applied only to slice 1, are summarized in Table 4.

The network dynamics shown in Figure 13 (panel A, middle) exhibit an initial transient oscillatory regime in the number of active pyramidal neurons across all slices, which eventually converges toward asymptotically persistent states. In contrast, the number of active interneurons in each slice rapidly reaches a stable equilibrium. As shown in Figure 16, after a short transient state, the activity of all

slices becomes influenced by the external stimulation, even though only slice 1 is directly targeted (see Figures S2–S5, middle and right panels). The dynamics arising in slices 2, 3, and 4 are thus entirely mediated by their connectivity with slice 1, as specified in Table 2 (top left). Oscillatory patterns persist around the asymptotically stable equilibria both at the whole-network scale (see Figures S2–S5, left panels) and within each individual slice (see Figures S2–S5, middle and right panels). However, in slices 3 and 4 the oscillations in the number of active interneurons appear markedly attenuated. This attenuation is due, on the one hand, to the weaker connectivity of slices 3 and 4 with slice 1 and, on the other hand, to the fact that during the transient state of the unperturbed dynamics the number of active interneurons has already reached its asymptotic value and is therefore less susceptible to significant variations.

Table 4. External inputs. The table reports the parameters used to simulate the arrival of external inputs in both the one- and four-slice network models (see Figures 15, 16, and S1–S5).

Panel	t_h	$\eta_I(t_h)$	$\eta_E(t_h)$
A	$0.8\,h, \quad h \in N$	0.15	0.15
B	$0.8\,h, \quad h \in N$	$0.3\left[\sin\left(10^7\,t_h\right)\right]^{12}$	$0.3\left[\sin\left(10^7\,t_h\right)\right]^{12}$
C	$t_0 = 1, \quad t_h = \begin{cases} t_{h-1} + 0.5 & h \mod 4 \neq 0, \\ t_{h-1} + 1 & h \mod 4 = 0, \end{cases} \quad h > 0$	0.15	0.15
D	random	$0.3\left[\sin\left(10^7\,t_h\right)\right]^{12}$	$0.3\left[\sin\left(10^7\,t_h\right)\right]^{12}$

In all scenarios, Figures S2–S5 show the dynamics of both the whole network and each individual slice, and additionally compare the intrinsic dynamics (dashed lines, no external input) with the externally driven dynamics (solid lines), in terms of the fraction of active interneurons and pyramidal neurons.

4. Conclusions and research perspectives

In this paper, we have employed a kinetic modeling approach to describe the evolution of a heterogeneous neuronal network composed of interneurons and pyramidal neurons. Specifically, the connectivity of the network— structured into S slices— is modeled through adjacency matrices, which act as weight functions, while neuronal interactions are described by transition probabilities.

This framework captures both intra-slice and inter-slice interactions, thus accounting for network heterogeneity in terms of connectivity structure and functionality. After deriving the general models (2.17) and (2.18), we analyzed three specific quasi-heterogeneous networks in which adjacency matrices and transition probabilities depend solely on whether neurons belong to the same slice or different ones. For the one-slice network, we also carried out an analytical investigation of coexistence equilibria and their stability properties. We then examined the two-slice and four-slice networks. Even within this simplified framework, the adjacency matrices and transition probabilities account for different dynamical behaviors driven by network heterogeneity. Furthermore, we introduced the inhibitory-count-dominated and excitatory-count-dominated regimes and proposed a criterion — based on inhibition- and excitation-count rates — to determine a priori which regime a network operates in. Although analytically proven only for the one-slice network, this regime identification is consistently confirmed by all numerical simulations. Our results demonstrate that increasing heterogeneity in the network modulates the fraction of active neurons and promotes the emergence of more complex

dynamical behaviors. This heterogeneity may potentially drive regime shifts between excitatory-count and inhibitory-count dominance. Finally, we investigated the effect of external inputs, modeled by redefining the initial state of the network during its time evolution and selectively activating fractions of interneurons and/or pyramidal neurons at specific time steps. This analysis revealed the emergence of distinct network regimes and oscillatory behaviors, while preserving the mathematical well-posedness of the system.

As future research directions, we aim to extend the framework (2.17) and (2.18) to a more general case, where the transition probabilities follow suitable distributions to account for the firing dynamics of adapting, non-adapting, and bursting neurons. Additionally, we plan to implement adjacency matrices that reproduce the biophysical connectivity reported in the literature [14, 52, 72]. Moreover, including external inputs directly in the model equations may complement the preliminary analysis presented in Subsection 3.4. Furthermore, we plan to perform mathematical and numerical analyses to characterize the dynamical behavior of neuronal networks, accounting for phenomena such as traveling waves, oscillations, and other emergent dynamics. Introducing time-dependent transition probabilities, accounting for synaptic plasticity, represents a future challenge for this framework. However, this extension may compromise some of the mathematical properties of the current model. We plan to introduce a continuous activity variable v representing the membrane potential and taking values in a continuous subset of $\mathbb{R}$. This would lead to a continuous kinetic framework, in which the system evolves according to a system of nonlinear partial-integro-differential equations. Beyond the mathematical challenge, this extension would enable the explicit modeling of membrane potential dynamics, providing a more physiologically realistic description of neuronal activity. In this context, a Fokker–Planck-type system could be derived under a quasi-invariant collision regime [74]. Furthermore, by extending the model to continuous membrane potential variables, we also aim to establish conceptual links with seminal mean-field theories by Amari [75, 76] on random analog networks and self-organizing binary threshold systems, which, like our framework, adopt a mesoscopic perspective to describe emergent collective dynamics. This extension would also facilitate the inclusion of synaptic plasticity or Hebbian-like adaptations of transition probabilities, thereby enabling the modeling of associative-memory mechanisms.

Finally, in line with the spatially structured slices considered in this study, we aim to introduce a continuous spatial variable representing the position of each neuron within the network. As with the continuous activity variable, this extension is expected to pose additional mathematically demanding challenges.

Use of AI tools declaration

The authors declare they have not used Artificial Intelligence (AI) tools in the creation of this article.

Acknowledgments

This paper has been funded by the Italian National Recovery and Resilience Plan (NRRP), M4C2, funded by the European Union – NextGenerationEU (Project IR0000011, CUP B51E22000150006, EBRAINS-Italy), by the EU Horizon Europe Program under the specific Grant Agreement 101147319, EBRAINS 2.0 project, and by the Italian National Recovery and Resilience Plan (NRRP), M4C2,

funded by the European Union – NextGenerationEU PRIN2022 (Project 2022ZY5RXB, CUP B53D23019160006, HIPPOCOMP). A. M. and M. M. acknowledge membership of the INdAM-GNFM Group. They thank Alessia Bonafede for technical and administrative assistance.

Conflict of interest

The authors declare there is no conflict of interest.

References

1. S. Dura-Bernal, B. Herrera, C. Lupascu, B. M. Marsh, D. Gandolfi, A. Marasco, et al., Large-scale mechanistic models of brain circuits with biophysically and morphologically detailed neurons, *J. Neurosci.*, **44** (2024), e1236242024. https://doi.org/10.1523/JNEUROSCI.1236-24.2024
2. D. Golomb, C. Yue, Y. Yaari, Contribution of persistent Na+ current and M-type K+ current to somatic bursting in CA1 pyramidal cells: combined experimental and modeling study, *J. Neurophysiol.*, **96** (2006), 1912–1926. https://doi.org/10.1152/jn.00205.2006
3. D. Bianchi, A. Marasco, A. Limongiello, C. Marchetti, H. Marie, B. Tirozzi, et al., On the mechanisms underlying the depolarization block in the spiking dynamics of CA1 pyramidal neurons, *J. Comput. Neurosci.*, **33** (2012), 207–225. https://doi.org/10.1007/s10827-012-0383-y
4. R. Migliore, C. A. Lupascu, L. L. Bologna, A. Romani, J. Courcol, S. Antonel, et al., The physiological variability of channel density in hippocampal CA1 pyramidal cells and interneurons explored using a unified data-driven modeling workflow, *PLoS Comput. Biol.*, **14** (2018), e1006423. https://doi.org/10.1371/journal.pcbi.1006423
5. D. Cai, L. Tao, A. V. Rangan, D. W. McLaughlin, Kinetic theory for neuronal network dynamics, *Commun. Math. Sci.*, **4** (2006), 97–127.
6. A. V. Rangan, G. Kovačič, D. Cai, Kinetic theory for neuronal networks with fast and slow excitatory conductances driven by the same spike train, *Phys. Rev. E: Stat. Nonlinear Soft Matter Phys.*, **77** (2008), 041915. https://doi.org/10.1103/PhysRevE.77.041915
7. A. Ferrara, D. Angulo-Garcia, A. Torcini, S. Olmi, Population spiking and bursting in next-generation neural masses with spike-frequency adaptation, *Phys. Rev. E*, **107** (2023), 024311. https://doi.org/10.1103/PhysRevE.107.024311
8. E. Montbrió, D. Pazó, A.Roxin, Macroscopic description for networks of spiking neurons, *Phys. Rev. X*, **5** (2015), 021028. https://doi.org/10.1103/PhysRevX.5.021028
9. G. Kovačič, L. Tao, A. V Rangan, D. Cai, Fokker-Planck description of conductance-based integrate-and-fire neuronal networks, *Phys. Rev. E: Stat. Nonlinear Soft Matter Phys.*, **80** (2009), 021904. https://doi.org/10.1103/PhysRevE.80.021904
10. L. Chen, S. A. Campbell, Exact mean-field models for spiking neural networks with adaptation, *J. Comput. Neurosci.*, **50** (2022), 445–469. https://doi.org/10.1007/s10827-022-00825-9
11. J. D. Kopsick, C. Tecuatl, K. Moradi, S. M. Attili, H. J. Kashyap, J. Xing, et al., Robust resting-state dynamics in a large-scale spiking neural network model of area CA3 in the mouse hippocampus, *Cognit. Comput.*, **15** (2023), 1190–1210. https://doi.org/10.1007/s12559-021-09954-2

12. A. Marasco, C. Tribuzi, A. Iuorio, M. Migliore, Mathematical generation of data-driven hippocampal CA1 pyramidal neurons and interneurons copies via A-GLIF models for large-scale networks covering the experimental variability range, *Math. Biosci.*, **371** (2024a), 109179. https://doi.org/10.1016/j.mbs.2024.109179

13. A. Marasco, C. Tribuzi, C. A. Lupascu, M. Migliore, Modeling realistic synaptic inputs of CA1 hippocampal pyramidal neurons and interneurons via adaptive generalized leaky integrate-and-fire models, *Math. Biosci.*, **372** (2024b), 109192. https://doi.org/10.1016/j.mbs.2024.109192

14. E. Spera, Intrinsic network dynamics in a full-scale point-neuron model of the CA1 hippocampal microcircuit incorporating excitability heterogeneity through multiple realistic A-GLIF instantiations, *in preparation.*

15. N. Brunel, Dynamics of sparsely connected networks of excitatory and inhibitory spiking neurons, *J. Comput. Neurosci.*, **8** (2000), 183–208. https://doi.org/10.1023/a:1008925309027

16. Q. L. Gu, S. Li, W. P. Dai, D. Zhou, D. Cai, Balanced active core in heterogeneous neuronal networks, *Front. Comput. Neurosci.*, **12** (2019), 109. https://doi.org/10.3389/fncom.2018.00109 .

17. C. van Vreeswijk, H. Sompolinsky, Chaotic balanced state in a model of cortical circuits, *Neural Comput.*, **10** (1998), 1321–1371. https://doi.org/10.1162/089976698300017214

18. Z. C. Xiao, K. K Lin, L. S. Young, A data-informed mean-field approach to mapping of cortical parameter landscapes, *PLOS Comput. Biol.*, **17** (2021), e1009718. https://doi.org/10.1371/journal.pcbi.1009718

19. Y. Zerlaut, S. Chemla, F. Chavane, A. Destexhe, Modeling mesoscopic cortical dynamics using a mean-field model of conductance-based networks of adaptive exponential integrate-and-fire neurons, *J. Comput. Neurosci.*, **44** (2018), 45–61. https://doi.org/10.1007/s10827-017-0668-2

20. R. Gast, S. A. Solla, A. Kennedy, Neural heterogeneity controls computations in spiking neural networks, *Proc. Natl. Acad. Sci.*, **121** (2024), e2311885121. https://doi.org/10.1073/pnas.2311885121

21. R. Gast, H. Schmidt, T. R Knösche, A mean-field description of bursting dynamics in spiking neural networks with short-term adaptation, *Neural Comput.*, **32** (2020), 1615–1634. https://doi.org/10.1162/neco_a_01300

22. G. Gigante, M. Mattia, P. D. Giudice, Diverse population-bursting modes of adapting spiking neurons, *Phys. Rev. Lett.*, **98** (2007), 148101. https://doi.org/10.1103/PhysRevLett.98.148101

23. W. Nicola, S. A. Campbell, Mean-field models for heterogeneous networks of two-dimensional integrate and fire neurons, *Front. Comput. Neurosci.*, **7** (2013), 184. https://doi.org/10.3389/fncom.2013.00184

24. M. Khanjanianpak, N. Azimi-Tafreshi, A. Valizadeh, Emergence of complex oscillatory dynamics in the neuronal networks with long activity time of inhibitory synapses, *iScience*, **27** (2024a), 109401. https://doi.org/10.1016/j.isci.2024.109401

25. T. Sasaki, N. Matsuki, Y. Ikegaya, Metastability of active CA3 networks, *J. Neurosci.*, **27** (2007), 517–528. https://doi.org/10.1523/JNEUROSCI.4514-06.2007

26. J. Pretel, V. Buendía, J. J. Torres, M. A. Muñoz, From asynchronous states to Griffiths phases and back: Structural heterogeneity and homeostasis in excitatory-inhibitory networks, *Phys. Rev. Res.*, **6** (2024), 023018. https://doi.org/10.1103/PhysRevResearch.6.023018
27. R. C. López, V. Buendía, M. A. Muñoz, Excitatory-inhibitory branching process: A parsimonious view of cortical asynchronous states, excitability, and criticality, *Phys. Rev. Res.*, **4** (2022), L042027. https://doi.org/10.1103/PhysRevResearch.4.L042027
28. T. Murakami, Spatial dynamics of spontaneous activity in the developing and adult cortices, *Neurosci. Res.*, **212** (2025), 1–10. https://doi.org/10.1016/j.neures.2024.12.002
29. D. B. Larremore, W. L. Shew, E. Ott, F. Sorrentino, J. G. Restrepo, Inhibition causes ceaseless dynamics in networks of excitable nodes, *Phys. Rev. Lett.*, **112** (2014a) 138103. https://doi.org/10.1103/PhysRevLett.112.138103
30. M. Di Volo, A. Destexhe, Optimal responsiveness and information flow in networks of heterogeneous neurons, *Sci. Rep.*, **11** (2022), 1–11.
31. C. G. Fink, Simulating synchronization in neuronal networks, *Am. J.Phys.*, **84** (2016), 467–473. https://doi.org/10.1119/1.4945009
32. D. J. Watts, S. H. Strogatz, Collective dynamics of 'small-world' networks, *Nature*, **393** (1998), 440–442.
33. E. Bullmore, O. Sporns, Complex brain networks: Graph theoretical analysis of structural and functional systems, *Nat. Rev. Neurosci.*, **10** (2009), 186–198.
34. F. V. Farahani, W. Karwowski, N. R. Lighthall, Application of graph theory for identifying connectivity patterns in human brain networks: A systematic review, *Front. Neurosci.*, **13** (2019), 439505. https://doi.org/10.3389/fnins.2019.00585
35. O. Sporns, Graph theory methods: Applications in brain networks, *Dialogues Clin. Neurosci.*, **20** (2018), 111–121. https://doi.org/10.31887/DCNS.2018.20.2/osporns
36. A. L. Barabási, R. Albert, Emergence of scaling in random networks, *Science*, **286** (1999), 509–512. https://doi.org/10.1126/science.286.5439.509
37. M. Khanjanianpak, A. Valizadeh, Optimizing information capacity in modular neural networks through excitatory and inhibitory connectivity, *Neurocomputing*, **640** (2025), 130313. https://doi.org/10.1016/j.neucom.2025.130313
38. J. Banasiak, A. Błoch, Telegraph systems on networks and port-Hamiltonians. II. Network realizability, *Networks Heterogen. Media*, **17** (2022), 73–99.
39. A. Barrat, M. Barthelemy, A. Vespignani, *Dynamical Processes on Complex Networks*, Cambridge University Press, 2008.
40. J. Gao, N. Yang, Some bounds on the largest eigenvalue of degree-based weighted adjacency matrix of a graph, *Discrete App. Math.*, **356** (2024), 21–31. https://doi.org/10.1016/j.dam.2024.05.011
41. N. Bellomo, D. Burini, N. Outada, Multiscale models of Covid-19 with mutations and variants, *Networks & Heterogen. Media*, **17** (2022), 293–310. https://doi.org/10.3934/nhm.2022008
42. N. Bellomo, D. Burini, G. Dosi, L. Gibelli, D. Knopoff, N. Outada, et al., What is life? A perspective of the mathematical kinetic theory of active particles, *Math. Models Methods Appl. Sci.*, **31** (2021), 1821–1866. https://doi.org/10.1142/S0218202521500408

43. N. Bellomo, A. Bellouquid, J. Nieto, J. Soler, Multiscale biological tissue models and flux-limited chemotaxis for multicellular growing systems, *Math. Models Methods Appl. Sci.*, **20** (2010), 1179–1207. https://doi.org/10.1142/S0218202510004568

44. A. Bellouquid, M. Delitala, Mathematical methods and tools of kinetic theory towards modelling complex biological systems, *Math. Models Methods Appl. Sci.*, **15** (2005), 1639–1666. https://doi.org/10.1142/S0218202505000923

45. M. J. Cáceres, J. A. Carrillo, L. Tao, A numerical solver for a nonlinear Fokker–Planck equation representation of neuronal network dynamics, *J.Comput. Phys.*, **230** (2011), 1084–1099. https://doi.org/10.1016/j.jcp.2010.10.027

46. B. Perthame, D. Salort, Derivation of a voltage density equation from a voltage-conductance kinetic model for networks of integrate-and-fire neurons, *Commun. Math. Sci.*, **17** (2019), 1193–1211. https://doi.org/10.4310/CMS.2019.v17.n5.a2

47. K. D. Harris, G. M. G. Shepherd, The neocortical circuit: Themes and variations, *Nature Neurosci.*, **18** (2015), 170–181.

48. A. M. Bastos, W. M. Usrey, R. A. Adams, G. R. Mangun, P. Fries, K. J. Friston, Canonical microcircuits for predictive coding, *Neuron*, **76** (2012), 695–711. https://doi.org/10.1016/j.neuron.2012.10.038

49. A. H. Gittis, A. C Kreitzer, Striatal microcircuitry and movement disorders, *Trends Neurosci.*, **35** (2012), 557–564. https://doi.org/10.1016/j.tins.2012.06.008

50. B. Hangya, H. J. Pi, D. Kvitsiani, S. P. Ranade, A. Kepecs, From circuit motifs to computations: Mapping the behavioral repertoire of cortical interneurons, *Curr. Opin. Neurobiol.*, **26** (2014), 117–124. https://doi.org/10.1016/j.conb.2014.01.007

51. M. Khona, I. R. Fiete, Attractor and integrator networks in the brain, *Nature Rev. Neurosci.*, **23** (2022), 744–766. https://doi.org/10.1038/s41583-022-00642-0

52. D. Gandolfi, J. Mapelli, S. Solinas, R. De Schepper, A. Geminiani, C. Casellato, et al., A realistic morpho-anatomical connection strategy for modelling full-scale point-neuron microcircuits, *Sci. Rep.*, **12** (2022), 246–276. https://doi.org/10.1038/s41598-022-18024-y

53. M. L. Schiavo, Discrete kinetic cellular models of tumors immune system interactions, *Math. Models Methods Appl. Sci.*, **6** (1996), 1187–1209. https://doi.org/10.1142/S021820259600050X

54. M. L. Bertotti, M. Delitala, On a discrete generalized kinetic approach for modelling persuader's influence in opinion formation processes, *Math. Comput. Modell.*, **48** (2008), 1107–1121. https://doi.org/10.1016/j.mcm.2007.12.021

55. A. Bellouquid, E. De Angelis, From kinetic models of multicellular growing systems to macroscopic biological tissue models, *Nonlinear Anal. Real World Appl.*, **12** (2011), 1111–1122. https://doi.org/10.1016/j.nonrwa.2010.09.005

56. D. Burini, N. Chouhad, Hilbert method toward a multiscale analysis from kinetic to macroscopic models for active particles, *Math. Models Methods Appl. Sci.*, **27** (2017), 1327–1353. https://doi.org/10.1142/S0218202517400176

57. R. C. López, V. Buendía, M. A. Muñoz, Excitatory-inhibitory branching process: A parsimonious view of cortical asynchronous states, excitability, and criticality, *Phys. Rev. Res.*, **4** (2022), L042027. https://doi.org/10.1103/PhysRevResearch.4.L042027

58. L. M. van Kessenich, D. Berger, L. de Arcangelis, H. J. Herrmann, Pattern recognition with neuronal avalanche dynamics, *Phys. Rev. E*, **99** (2019), 010302. https://doi.org/10.1103/PhysRevE.99.010302

59. D. B. Larremore, W. L. Shew, E. Ott, F. Sorrentino, J. G. Restrepo, Inhibition causes ceaseless dynamics in networks of excitable nodes, *Phys. Rev. Lett.*, **112** (2014b), 138103. https://doi.org/10.1103/PhysRevLett.112.138103

60. A. V. Goltsev, F. V. De Abreu, S. N. Dorogovtsev, J. F. F. Mendes, Stochastic cellular automata model of neural networks, *Phys. Rev. E*, **81** (2010), 061921. https://doi.org/10.1103/PhysRevE.81.061921

61. J. D. Cowan, J. Neuman, W. van Drongelen, Wilson–Cowan equations for neocortical dynamics, *J. Math. Neurosci.*, **6** (2016), 1. https://doi.org/10.1186/s13408-015-0034-5

62. J. Pérez-Ortega, T. Alejandre-García, R. Yuste, Long-term stability of cortical ensembles, *Elife*, **10** (2021), e64449. https://doi.org/10.7554/eLife.64449

63. P. Theodoni, G. Kovács, M. W. Greenlee, G. Deco, Neuronal adaptation effects in decision making, *J. Neurosci.*, **31** (2011), 234–246. https://doi.org/10.1523/JNEUROSCI.2757-10.2011

64. C. D. Verdugo, S. Myren-Svelstad, E. Aydin, E. Van Hoeymissen, C. Deneubourg, S. Vanderhaeghe, et al., Glia-neuron interactions underlie state transitions to generalized seizures, *Nature Commun.*, **10** (2019), 3830. https://doi.org/10.1038/s41467-019-11739-z

65. S. Fernández-García, J. G. Orlandi, G. A. García-Díaz Barriga, M. J. Rodríguez, M Masana, J. Soriano, et al., Deficits in coordinated neuronal activity and network topology are striatal hallmarks in Huntington's disease, *BMC Biol.*, **18** (2020), 58. https://doi.org/10.1186/s12915-020-00794-4

66. N. Brunel, Storage capacity of neural networks: Effect of the fluctuations of the number of active neurons per memory, *J. Phys. A: Math. Gen.*, **27** (1994), 4783. https://doi.org/10.1088/0305-4470/27/14/009

67. E. Estévez-Priego, M. Moreno-Fina, E. Monni, Z. Kokaia, J. Soriano, D. Tornero, Long-term calcium imaging reveals functional development in hiPSC-derived cultures comparable to human but not rat primary cultures, *Stem Cell Rep.*, **18** (2005), 205–219. https://doi.org/10.1016/j.stemcr.2022.11.014

68. K. Blinowska, G. Müller-Putz, V. Kaiser, L. Astolfi, K. Vanderperren, S. Van Huffel, et al., Multimodal imaging of human brain activity: Rational, biophysical aspects and modes of integration, *Comput. Intell. Neurosci.*, **1** (2009), 813607. https://doi.org/10.1155/2009/813607

69. M. L. Bertotti, M. Delitala, From discrete kinetic and stochastic game theory to modelling complex systems in applied sciences, *Math. Models Methods Appl. Sci.*, **14** (2004),1061–1084. https://doi.org/10.1142/S0218202504003544

70. A. Marasco, E. Spera, V. De Falco, A. Iuorio, C. A. Lupascu, S. Solinas, et al., An adaptive generalized leaky integrate-and-fire model for hippocampal CA1 pyramidal neurons and interneurons, *Bull. Math. Biol.*, **85** (2023), 109. doi: https://doi.org/10.1007/s11538-023-01206-8

71. M. Khanjanianpak, N. Azimi-Tafreshi, A. Valizadeh, Emergence of complex oscillatory dynamics in the neuronal networks with long activity time of inhibitory synapses, *Iscience*, **27** (2024b), 109401. https://doi.org/10.1016/j.isci.2024.109401

72. D. Gandolfi, J. Mapelli, S. M. G. Solinas, P. Triebkorn, E. D'Angelo, V. Jirsa, et al., Full-scale scaffold model of the human hippocampus CA1 area, *Nature Comput. Sci.*, **3** (2023), 264–276. https://doi.org/10.1038/s43588-023-00417-2

73. C. Godsil, G. F. Royle, *Algebraic Graph Theory*, Springer Science & Business Media, 2013.

74. L. Pareschi, G. Toscani, *Interacting Multiagent Systems: Kinetic Equations and Monte Carlo Methods*, OUP Oxford, 2013.

75. S. I. Amari, Characteristics of random nets of analog neuron-like elements, *IEEE Trans. Syst. Man Cybern.*, **SMC-2** (1972a), 643–657. https://doi.org/10.1109/TSMC.1972.4309193

76. S. I. Amari, Learning patterns and pattern sequences by self-organizing nets of threshold elements, *IEEE Trans, Comput,*, **C-21** (1972b), 1197–1206. https://doi.org/10.1109/T-C.1972.223477

AIMS Press